

Fault Tolerant Control for the Flying-V Using Adaptive Incremental Nonlinear Dynamic Inversion

Atmaca, D.; van Kampen, E.

DOI

[10.2514/6.2025-0081](https://doi.org/10.2514/6.2025-0081)

Publication date

2025

Document Version

Final published version

Published in

AIAA Science and Technology Forum and Exposition, AIAA SciTech Forum 2025

Citation (APA)

Atmaca, D., & van Kampen, E. (2025). Fault Tolerant Control for the Flying-V Using Adaptive Incremental Nonlinear Dynamic Inversion. In *AIAA Science and Technology Forum and Exposition, AIAA SciTech Forum 2025* Article AIAA 2025-0081 (AIAA Science and Technology Forum and Exposition, AIAA SciTech Forum 2025). American Institute of Aeronautics and Astronautics Inc. (AIAA).
<https://doi.org/10.2514/6.2025-0081>

Important note

To cite this publication, please use the final published version (if applicable).
Please check the document version above.

Copyright

Other than for strictly personal use, it is not permitted to download, forward or distribute the text or part of it, without the consent of the author(s) and/or copyright holder(s), unless the work is under an open content license such as Creative Commons.

Takedown policy

Please contact us and provide details if you believe this document breaches copyrights.
We will remove access to the work immediately and investigate your claim.



Fault Tolerant Control for the Flying-V Using Adaptive Incremental Nonlinear Dynamic Inversion

Direnc Atmaca* and Erik-Jan van Kampen†

Delft University of Technology, Kluyverweg 1, 2629 HS, Delft, The Netherlands

The Flying-V emerges as a unique flying wing type commercial aircraft design, distinguished by its V-shaped configuration. For such unconventional airframes, flight control systems are vital for ensuring safety and enhancing flight performance. Current Flying-V control systems primarily use incremental nonlinear dynamic inversion (INDI), a sensor-based feedback linearization method requiring an onboard control effectiveness model. Although INDI handles model uncertainties, significant mismatches between actual and onboard models caused by damages or faults degrade performance and compromise flight safety. This study proposes an adaptive strategy for incremental nonlinear dynamic inversion, employing an online two-step method to estimate changes in the aircraft's control effectiveness. Estimates are used to update the onboard control effectiveness model to minimize the mismatch between the actual and onboard representation of control effectiveness.

I. Introduction

According to the International Energy Agency, the aviation sector caused 2% of all CO₂ emissions in 2022*. This number may not seem significant; however, on a global scale it is sufficient to harbor the concern of regulatory bodies. Recently, the International Air Transport Association outlined its commitment and road map to achieve net-zero carbon emissions by 2050 †. Turning this commitment into reality will require the combined effort of the entire aviation community, including airlines, manufacturers, and academia.

To this end, many government, private, and academic initiatives prioritize exploring new aircraft designs and propulsion technologies. One example of such an initiative is the Flying-V aircraft, which was proposed in [1] at Airbus. The Flying-V is a long-distance efficient design that promises up to 20% fuel efficiency improvement over conventional aircraft‡. The benefit of the Flying-V comes from its distinctive V-shaped airframe that produces considerably lower drag than traditional tube and wing configurations.

As a new aircraft design, one major question surrounding the Flying-V is flight safety. Although the ability to withstand structural and actuator faults is imperative for all aircraft, this is particularly important for the Flying-V, since recent studies on handling qualities revealed insufficient control authority under certain conditions [2–4]. Combining this with a control surface failure can have devastating consequences on flight safety. Hence, integrating fault-tolerant flight control systems is essential for the future of the Flying-V as they allow investigating the effect of various faults and the development of strategies to mitigate them.

The current Flight Control System (FCS) of the Flying-V is based on Incremental Nonlinear Dynamic Inversion (INDI) with a Flight Envelope Protection (FEP) system. This control system was proposed in [5], as an improvement to the initial flight control design suggested in [6]. The existing flight control system uses an Airbus inspired C* longitudinal controller together with a roll rate and sideslip command for lateral-directional control. The FCS accounts for sensor noise, delays, and actuator dynamics while managing to provide level 1 handling qualities. This controller was recently tested in the SIMONA Research Simulator of TU Delft with real airline test pilots. The handling qualities were found to be between level 1 and level 2 for most conditions [2]. In addition, thanks to the INDI inner loop, the FCS is shown to be robust up to 20% uncertainty between the actual aircraft and the onboard control effectiveness (CE) model. However, for larger uncertainties, the performance of the INDI starts to degrade. This poses a problem for fault tolerance, as actuator faults or structural damage can lead to significant deviations between the real aircraft and the

*PhD Candidate, Control and Simulation, Faculty of Aerospace Engineering, AIAA Student Member

†Associate Professor, Control and Simulation, Faculty of Aerospace Engineering

*<https://www.iea.org/energy-system/transport/aviation#tracking>

†<https://www.iata.org/en/programs/environment/flynetzero/>

‡<https://www.tudelft.nl/en/ae/flying-v>

onboard model. In fact, a recent study showed that under severe damage, regular INDI can no longer satisfy closed-loop stability [7].

To solve this problem, this paper proposes an Adaptive INDI method that relies on online two-step state and parameter estimation to update the onboard model during flight. Adaptive INDI has been previously applied to a variety of aerospace problems. In [8], an Adaptive INDI with online control effectiveness estimation is proposed for attitude control of micro aerial vehicles. The success of the method is demonstrated with real-world experiments in which the controller manages to cope with changes in control effectiveness within the flight envelope and maintains high performance and disturbance rejection properties. Another study [9] applies Adaptive INDI to obtain consistent handling qualities under CE uncertainties and center-of-gravity shifts for an F-16 aircraft model. The estimation process manages to lower handling quality variations and allows for a more stable flight. However, both of these applications rely on least-mean-squares (LMS) for online CE estimation. Instead of LMS, this paper uses recursive least squares with variable forgetting factor (VFF-RLS). Under fault conditions, RLS is a better alternative as it has faster convergence properties and can dynamically change the aggressiveness of adaptation due to the variable forgetting factor. Furthermore, RLS will adapt faster after a damage or fault, which is critical because flight safety depends heavily on the speed of adaptation under post-damage conditions.

This paper offers three main contributions. First, it proposes a fault-tolerant flight control architecture with an Adaptive INDI inner loop. Secondly, it implements a two-step state and parameter estimation scheme for online control effectiveness estimation, where the state estimation employs Extended Kalman Filter with an air-data-based kinematic model, while parameter estimation is carried out using recursive least squares with a variable forgetting factor. Lastly, it provides a comparative analysis of different onboard control effectiveness models, examining their influence on maneuverability after structural damage and, by extension, flight safety.

Section II focuses on the simulation model of the Flying-V, including the aerodynamic model, control surfaces, and sensors. Section III presents the complete control architecture that outlines the inner and outer loop control laws. Section IV describes the model configurations, tracking signals, and the simulation timeline. Section V presents the simulation results for a variety of model configurations. Finally, Section VI provides a conclusion and suggests directions for future research.

II. The Flying-V Aircraft

This section introduces the Flying-V simulation model that includes the aerodynamic model, control surface layout, actuator dynamics, and sensors. The Flying-V is under constant development; consequently, there are many design iterations with different aerodynamic and structural characteristics. The Flying-V model explained in this section uses the latest available structure of the aircraft.

A. Aerodynamic Model

The aerodynamic model comes from a synthesis of two different models generated through two different methods. The first model is based on the linear vortex lattice method (VLM) proposed in [10]. The VLM is able to provide an accurate model near the evaluation points. However, due to its linear structure, it cannot capture nonlinear phenomena such as pitch break. As a result, it is only valid for angle of attack values between -5 and 15 degrees. The second model is based on a wind tunnel experiment (WTE) performed on the scaled model of the Flying-V as outlined in [11]. This model is capable of capturing nonlinear effects and is valid up to 30 degrees angle of attack.

The synthesis of the final model is proposed and explained in [12]. Prior to the integration of the two models, the WTE model is scaled up to match the full-size aircraft. Following this, the two models are combined, where the VLM model covers the angle of attack range between -5 and 15 degrees, and WTE covers between 15 and 30 degrees. The issue of discontinuity arising from the integration of models at the angle of attack of 15 degrees is addressed through the application of cubic Hermite polynomial interpolation. The aerodynamic coefficients in the combined model are available for mach numbers $M = 0.85$ and $M = 0.2$. For all other cases, the coefficients are linearly interpolated between these two conditions.

B. Control Surfaces and Actuators

1. Control Layout

The layout of the control surfaces and their deflection limits are taken from [10], which is the same study that proposed the VLM model. Each wing contains two elevons and one rudder. Elevons are control surfaces that act as both elevator and aileron, so, they are used for both pitch and roll control. Rudders are commanded together with the same deflection angle. Consequently, excluding the engines, this configuration of the Flying-V has five control surfaces. Figure 1 presents the control layout and structure of the Flying-V, while Table 1 explains the labels for the control surfaces along with their respective position and rate limits.

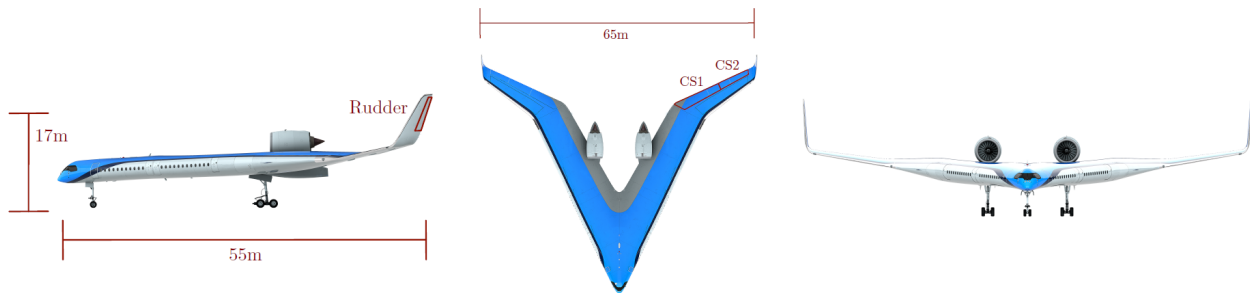


Fig. 1 Flying-V control layout, obtained from [6]

Table 1 Control surfaces and limits: rate limits are obtained from [5]

Label	Control Surface	Position Limit, deg	Rate Limit, deg/s
CS1 _L	Left inboard elevon	±25	±80
CS2 _L	Left outboard elevon	±25	±80
CS1 _R	Right inboard elevon	±25	±80
CS2 _R	Right outboard elevon	±25	±80
CS3	Rudders	±30	±120

2. Actuator Dynamics

The control surface actuators are modeled as a second-order high-bandwidth system. This actuator model was previously used in [5] and was initially suggested in [13]. Engines are modeled as a simple first-order system. Both of these systems are given in Equation 1.

$$H_{Act}(s) = \frac{(100)(40)}{(s+40)(s+100)} \quad \text{and} \quad H_{Eng}(s) = \frac{1}{0.2s+1} \quad (1)$$

The aircraft engine is selected to be Rolls-Royce Trent XWB-84. The thrust specifications of this engine are available in [14].

C. Sensors

The sensors used in the Flying-V simulation model come from a set of readily available options. The selection of these sensors is conducted with consideration of both the commercial application of the Flying-V and industry standards for airliners. To this end, a navigation grade inertial measurement unit (IMU) that is certified to operate without GPS/GNSS assistance is chosen. This IMU comes with three state-of-the-art gyroscopes and accelerometers, both of which have been widely used in aviation and have demonstrated their applicability in commercial aircraft. The air data system (ADS) specifications are based on the Cessna Citation II PH-LAB aircraft. This is a research aircraft jointly owned and operated by the Netherlands Aerospace Center (NLR) and the Delft University of Technology. These specifications were previously obtained and used in [5].

Table 2 Measured parameters and their characteristics

Measured parameter	Update rate, Hz	Noise level, σ	Bias	Unit
V_m	100	0.005	2.5	m/s
α_m, β_m	100	$2.7 \cdot 10^{-4}$	$3.0 \cdot 10^{-5}$	rad
ϕ_m, θ_m	100	$8.7 \cdot 10^{-5}$	-	rad
ψ_m	100	$1.7 \cdot 10^{-4}$	-	rad
A_{xm}, A_{ym}, A_{zm}	100	$6.9 \cdot 10^{-4}$	$2.5 \cdot 10^{-4}$	m/s ²
p_m, q_m, r_m	100	$4.1 \cdot 10^{-6}$	$1.7 \cdot 10^{-8}$	rad/s

Something these sensors do not provide, yet is critical for the INDI controller are the rotational accelerations $\dot{p}, \dot{q}, \dot{r}$. These are needed to perform a sensor-driven model inversion. Typically, rotational accelerations are not available directly from the sensors, unless the aircraft is equipped with angular accelerometers. Fortunately, they can be calculated from gyroscopes using first-order Euler differentiation. However, before that, the samples collected from the gyros must be filtered. This is an important step because any unfiltered noise will be amplified by the differentiation process and hinder the performance of the INDI controller. Figure 2 presents the schematic of the calculation procedure. Blue boxes show the gains, green boxes show discrete differentiators, yellow is a unit delay, and red is the sampling rate. The

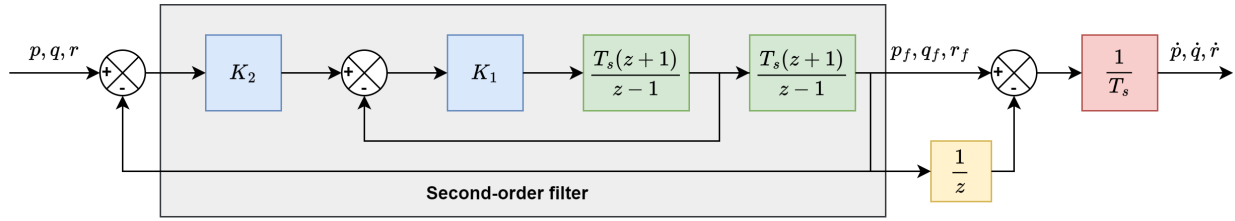


Fig. 2 Calculation schematic for angular accelerations, based on [5]

second order filter has a frequency $\omega_f = 30$ rad/s, and a damping ratio $\zeta_f = 1$, with a time step $T_s = 0.01s$ [5]. Based on this, the gains are given in equation 2.

$$K_1 = 2\omega_f\zeta_f \quad \text{and} \quad K_2 = \frac{\omega_f}{2\zeta_f} \quad (2)$$

Section III will discuss the design of the fault-tolerant flight control system, which comprises an inner loop based on Adaptive INDI with online parameter estimation and an outer loop utilizing an Airbus inspired C* controller in combination with roll rate and sideslip controllers.

III. Fault-Tolerant Flight Control Design

This section covers the complete control architecture of the Flying-V, as presented in Figure 3. The discussion is divided into three subsections. First, the core INDI structure and the control allocation algorithm is introduced. Secondly, the two-step method and its relation to the adaption scheme are addressed. Lastly, the outer loop control laws including the flight envelope protection are presented. The core INDI structure and the outer loop control laws that exclude online adaptation are based on the design suggested in [5], which drew initial inspiration from [15].

A. Incremental Nonlinear Dynamic Inversion and Cascaded Inverses

Incremental Nonlinear Dynamic Inversion (INDI) is a sensor-driven feedback linearization method. Unlike its model-based counterpart, Nonlinear Dynamic Inversion, INDI does not require a complete system model for control design. In the context of aircraft control, INDI only needs the control effectiveness matrix to invert the model, thereby linearizing the system. It is possible to derive an INDI control law, starting from the general nonlinear system given in Equation 3.

$$\dot{x} = f(x, u) \quad (3)$$

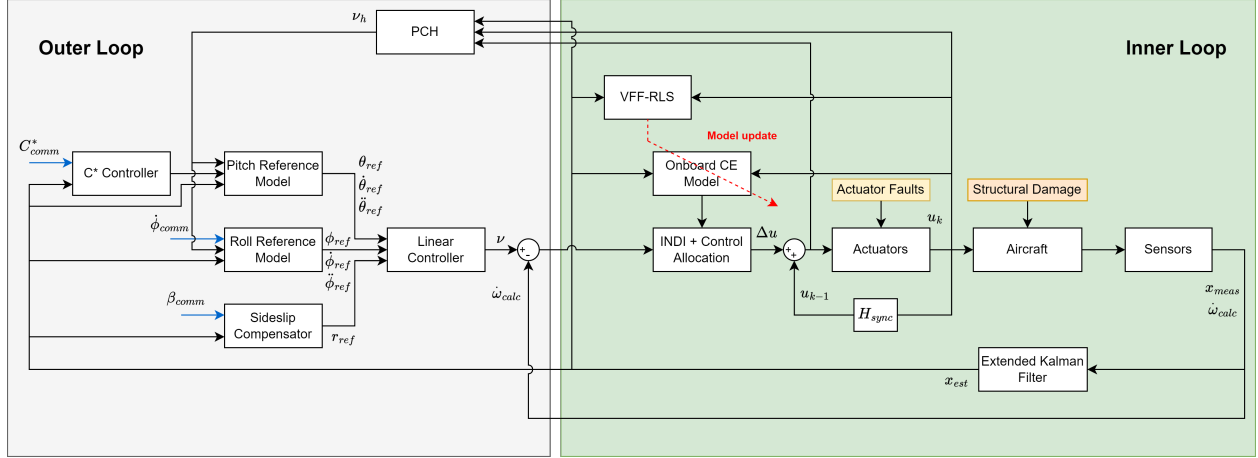


Fig. 3 Flight Control Architecture

This system can be linearized by taking the first-order Taylor series expansion at the current time step as

$$\begin{aligned} \dot{x} &\approx f(x_0, u_0) + \left. \frac{\partial f(x, u)}{\partial x} \right|_{x=x_0, u=u_0} (x - x_0) + \left. \frac{\partial f(x, u)}{\partial u} \right|_{x=x_0, u=u_0} (u - u_0) \\ &\approx \dot{x}_0 + \mathbf{F}(x_0, u_0) (x - x_0) + \mathbf{G}(x_0, u_0) (u - u_0) \end{aligned} \quad (4)$$

In Equation 4, \mathbf{F} refers to a matrix that contains the stability derivatives and \mathbf{G} the control derivatives. This linearized system can be simplified using the time-scale separation principle. Assuming that $\mathbf{F}(x_0, u_0) \Delta x \ll \mathbf{G}(x_0, u_0) \Delta u$, the contribution of the stability derivatives can be neglected. This assumption holds true when the actuators are sufficiently fast such that the controls change much faster than the states. The simplified system is given in Equation 5.

$$\Delta u = \mathbf{G}^{-1}(x_0, u_0) (\nu - \dot{x}_0) \quad (5)$$

In this expression, ν is called the virtual control input, and it stands for the time derivatives of the control variables, whereas \dot{x}_0 is assumed to be directly measured or calculated using measurements. For the purposes of this paper, INDI is applied to the body rate control problem. For this, the selected control variables (\mathbf{cv}) and their time derivatives are given in Equations 6 and 7, respectively.

$$\mathbf{cv}(x) = \begin{bmatrix} p & q & r \end{bmatrix}^T = \boldsymbol{\omega} \quad (6)$$

$$\frac{d\mathbf{cv}(x)}{dt} = \begin{bmatrix} v_p & v_q & v_r \end{bmatrix}^T = \dot{\boldsymbol{\omega}} \quad (7)$$

Therefore, by using the body rates as control variables, it is possible to write the incremental control law as the following:

$$\begin{bmatrix} \Delta \delta_{CS1L} \\ \Delta \delta_{CS1R} \\ \Delta \delta_{CS2L} \\ \Delta \delta_{CS2R} \\ \Delta \delta_{CS3} \end{bmatrix} = \mathbf{G}^{-1}(x, u) \left\{ \begin{bmatrix} v_p \\ v_q \\ v_r \end{bmatrix} - \begin{bmatrix} \dot{p} \\ \dot{q} \\ \dot{r} \end{bmatrix}_{calc} \right\} \quad (8)$$

Referring back to Figure 3, this incremental control input must be added to the previous control deflection to obtain the total control input. In Equation 8, the control derivative matrix has the following structure:

$$\mathbf{G}(x, u) = \bar{\rho} S c \mathbf{I}^{-1} \begin{bmatrix} C_{l\delta_{CS1L}} & C_{l\delta_{CS1R}} & C_{l\delta_{CS2L}} & C_{l\delta_{CS2R}} & C_{l\delta_{CS3}} \\ C_{m\delta_{CS1L}} & C_{m\delta_{CS1R}} & C_{m\delta_{CS2L}} & C_{m\delta_{CS2R}} & C_{m\delta_{CS3}} \\ C_{n\delta_{CS1L}} & C_{n\delta_{CS1R}} & C_{n\delta_{CS2L}} & C_{n\delta_{CS2R}} & C_{n\delta_{CS3}} \end{bmatrix} = \bar{\rho} S c \mathbf{I}^{-1} \mathbf{B} \quad (9)$$

where $\bar{\rho}$ is the dynamic pressure, S is the wing surface area, c is the mean aerodynamic chord, \mathbf{I} is the inertia matrix, and \mathbf{B} is the control effectiveness matrix. From Equation 8, it is clear that \mathbf{G} must be inverted. However, since there are only three moments and five control surfaces, the resulting system is under-determined. Therefore, the control effectiveness matrix is not square. This problem can be solved by employing a control allocation strategy. For that, Cascaded Generalized Inverses (CGI) [16] is chosen as the control allocation method. It was also used by [5] in a previous control design for the Flying-V, and is found to be effective. CGI relies on an unweighted Moore-Penrose pseudo-inverse for inverting the control effectiveness matrix. This pseudo-inverse is an optimal, minimum-norm method that minimizes the sum of squares of total control deflections. Hence, the inverse of the control effectiveness matrix can be written as

$$\mathbf{B}_{P_{inv}} = \mathbf{B}^T (\mathbf{B}\mathbf{B}^T)^{-1} \quad (10)$$

Using this, the final control input is given in Equation 11.

$$\Delta \mathbf{u} = \mathbf{B}_{P_{inv}} \frac{\mathbf{I}}{\bar{\rho} S c} (\mathbf{v} - \dot{\omega}_{calc}) \quad (11)$$

In addition to this inversion, CGI is also able to deal with control surface saturation. Before performing the pseudo-inverse, the CGI algorithm removes the associated columns and rows of all saturated control surfaces from the control effectiveness matrix (CEM). After this, the reduced CEM is reformulated and used to calculate the incremental control deflections.

B. Adaptive INDI Formulation Using State and Parameter Estimation

As explained in the previous section, INDI only requires a control effectiveness (CE) model of the aircraft to derive the control law. This model is stored onboard the aircraft and is typically made up of constant look-up tables. In an ideal scenario, the model will perfectly capture the actual control effectiveness of the aircraft. In reality, there will always be mismatches between actual and modeled CE. Fortunately, for this simulation model and control design, mismatches up to 20% can be tolerated [5]. However, if the mismatch is significant, INDI's performance deteriorates, possibly resulting in loss of control.

A large mismatch between models is likely to occur as a result of structural damage or actuator faults. To prevent such a discrepancy, this section introduces an adaptive approach for INDI that relies on online CE estimation using Recursive Least Squares with Variable Forgetting Factor (VFF-RLS). These estimates are used for updating the \mathbf{B} matrix, which guarantees that the controller has access to accurate, real-time information about changes in control effectiveness. This allows INDI to maintain its performance, thus ensuring safe flight conditions after damage.

The VFF-RLS approach involves taking sensor measurements to calculate the forces and moments acting on the aircraft, and to form a regression vector. Consequently, the accuracy of the method is highly dependent on sensor noise and bias. For this reason, before parameter estimation, an Extended Kalman Filter is implemented to utilize redundant but contaminated sensor information to obtain accurate state estimates. Figure 4 outlines the inner loop structure that includes true system dynamics, controller, state estimation, parameter estimation, and model update.

1. State Estimation Using Extended Kalman Filter

The Extended Kalman Filter (EKF) makes use of kinematic relations driven by IMU readings in combination with direct sensory measurements to obtain redundant information regarding the states of the aircraft. Since kinematic relations can be derived exactly, they provide robustness over aerodynamic models. Such kinematic models have been applied many times for joint state estimation and fault identification problems [17–20].

Consider a general nonlinear system in state-space form:

$$\dot{\mathbf{x}} = \mathbf{f}(\mathbf{x}(t), \mathbf{u}_m(t)) + \mathbf{N}(\mathbf{x}(t)) \boldsymbol{\omega}(t) \quad (12)$$

$$\mathbf{z}(t) = \mathbf{h}(\mathbf{x}(t), \mathbf{u}_m(t), t) \quad (13)$$

$$\mathbf{z}_m(t) = \mathbf{z}(t) + \mathbf{v}(t) \quad (14)$$

In this system, \mathbf{x} denotes the states, \mathbf{f} is a system of state equations, \mathbf{u}_m are the measured inputs, \mathbf{N} is the input noise distribution matrix, \mathbf{z} represents the measurement equations, and $\boldsymbol{\omega}$ and \mathbf{v} are the input and measurement noise vectors, respectively. Both of these noise vectors are zero-mean with a Gaussian distribution. The choice of \mathbf{f} depends on the states intended for estimation and the availability of direct sensor measurements of these states. For parameter

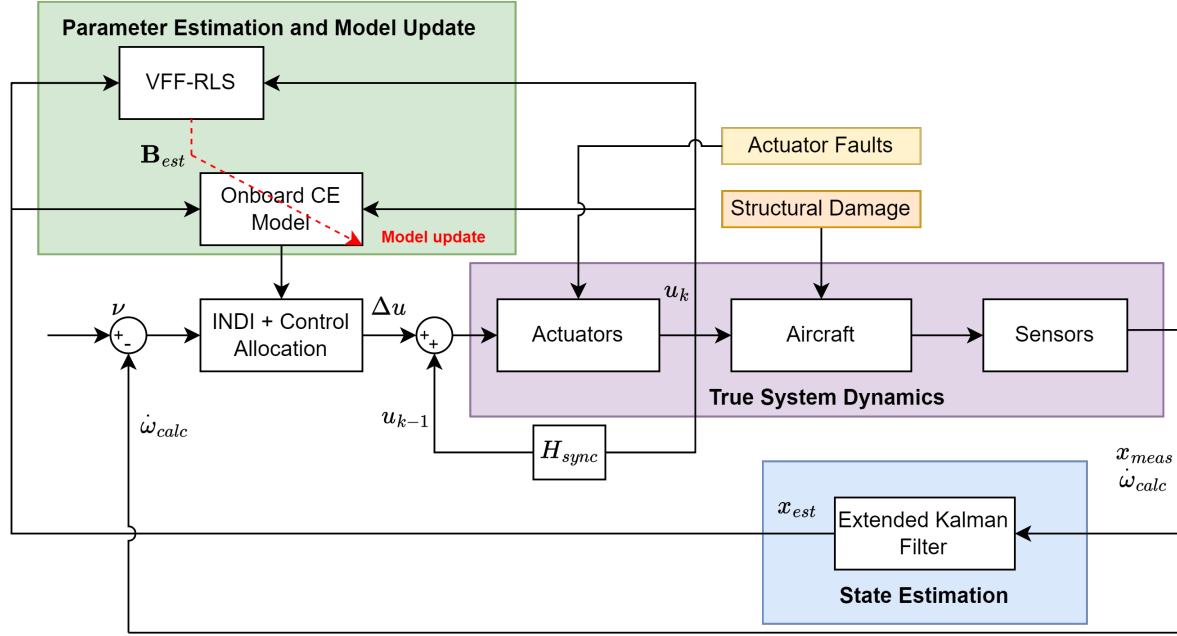


Fig. 4 Structure of the inner loop

estimation, it is clear that the regression vector given in Equation 37 requires accurate values for true airspeed, angle of attack, and sideslip. In addition, the outer loop controllers make use of roll, pitch, and yaw extensively for both reference signal generation and flight envelope protection. In light of this, an air data based kinematic model is chosen for state estimation, which leads to the following definitions for the nonlinear system:

$$\mathbf{x} = [V_t \quad \alpha \quad \beta \quad \phi \quad \theta \quad \psi]^T \quad (15)$$

$$\mathbf{u}_m = [A_{xm} \quad A_{ym} \quad A_{zm} \quad p_m \quad q_m \quad r_m]^T = [A_x \quad A_y \quad A_z \quad p \quad q \quad r]^T + \boldsymbol{\omega} \quad (16)$$

$$\mathbf{z}_m = [V_{tm} \quad \alpha_m \quad \beta_m \quad \phi_m \quad \theta_m \quad \psi_m]^T = [V_t \quad \alpha \quad \beta \quad \phi \quad \theta \quad \psi]^T + \mathbf{v} \quad (17)$$

$$\boldsymbol{\omega} = [\omega_{A_x} \quad \omega_{A_y} \quad \omega_{A_z} \quad \omega_p \quad \omega_q \quad \omega_r]^T \quad (18)$$

$$\mathbf{v} = [v_{V_t} \quad v_\alpha \quad v_\beta \quad v_\phi \quad v_\theta \quad v_\psi]^T \quad (19)$$

where V_t , α , β are the true airspeed, angle of attack, and sideslip angle. ϕ , θ , ψ are the Euler angles representing roll, pitch, and yaw. A_x , A_y , A_z are the linear accelerations, and p , q , r are the angular rates. Following this, the exact state equations are written as follows:

$$\dot{V}_t = (A_{xm} - \omega_{Ax}) \cos \alpha \cos \beta + (A_{ym} - \omega_{Ay}) \sin \beta + (A_{zm} - \omega_{Az}) \sin \alpha \cos \beta \quad (20)$$

$$\dot{\alpha} = \frac{1}{V \cos \beta} [-(A_{xm} - \omega_{Ax}) \sin \alpha + (A_{zm} - \omega_{Az}) \cos \alpha] \quad (21)$$

$$- [(p_m - \omega_p) \cos \alpha + (r_m - \omega_r) \sin \alpha] \tan \beta + (q_m - \omega_q)$$

$$\dot{\beta} = \frac{1}{V} [-(A_{xm} - \omega_{Ax}) \cos \alpha \sin \beta + (A_{ym} - \omega_{Ay}) \cos \beta - (A_{zm} - \omega_{Az}) \sin \alpha \sin \beta] \quad (22)$$

$$+ (p_m - \omega_p) \sin \alpha - (r_m - \omega_r) \cos \alpha$$

$$\dot{\phi} = (p_m - \omega_p) + (q_m - \omega_q) \sin \phi \tan \theta + (r_m - \omega_r) \cos \phi \tan \theta \quad (23)$$

$$\dot{\theta} = (q_m - \omega_q) \cos \phi - (r_m - \omega_r) \sin \phi \quad (24)$$

$$\dot{\psi} = (q_m - \omega_q) \frac{\sin \phi}{\cos \theta} + (r_m - \omega_r) \frac{\cos \phi}{\cos \theta} \quad (25)$$

Based on this, the input noise distribution matrix is defined as:

$$\mathbf{N}(x(t)) = \begin{bmatrix} -\cos \alpha \cos \beta & -\sin \beta & -\sin \alpha \cos \beta & 0 & 0 & 0 \\ \sin \alpha / (V \cos \beta) & 0 & -\cos \alpha / (V \cos \beta) & \cos \alpha \tan \beta & -1 & \sin \alpha \tan \beta \\ (\cos \alpha \sin \beta) / V & -\cos \beta / V & (\sin \alpha \sin \beta) / V & -\sin \alpha & 0 & \cos \alpha \\ 0 & 0 & 0 & -1 & -\sin \phi \tan \theta & -\cos \phi \tan \theta \\ 0 & 0 & 0 & 0 & -\cos \phi & \sin \phi \\ 0 & 0 & 0 & -1 & -\sin \phi / \cos \theta & -\cos \phi / \cos \theta \end{bmatrix} \quad (26)$$

Now that the kinematic model is defined, the next step is incorporating the Extended Kalman Filter, which is a non-optimal extension of the Kalman Filter to nonlinear systems. The steps of the EKF in discrete form are defined by the following set of equations [21]:

$$\hat{\mathbf{x}}_{k+1,k} = \hat{\mathbf{x}}_{k,k} + \int_{t_k}^{t_{k+1}} \mathbf{f}(\hat{\mathbf{x}}_{k,k}(t), \mathbf{u}_m(t)) dt \quad (27)$$

$$\hat{\mathbf{x}}_{k+1,k+1} = \hat{\mathbf{x}}_{k+1,k} + \mathbf{K}_{k+1} (\mathbf{z}_{m_{k+1}} - \mathbf{H}_k \hat{\mathbf{x}}_{k+1,k}) \quad (28)$$

$$\mathbf{P}_{k+1,k} = \mathbf{\Phi}_{k+1,k} \mathbf{P}_{k,k} \mathbf{\Phi}_{k+1,k}^T + \mathbf{\Gamma}_{k+1,k} \mathbf{Q}_{k,k} \mathbf{\Gamma}_{k+1,k}^T \quad (29)$$

$$\mathbf{K}_{k+1} = \mathbf{P}_{k+1,k} \mathbf{H}_k^T (\mathbf{H}_k \mathbf{P}_{k+1,k} \mathbf{H}_k^T + \mathbf{R}_{k+1})^{-1} \quad (30)$$

$$\mathbf{P}_{k+1,k+1} = (\mathbf{I} - \mathbf{K}_{k+1} \mathbf{H}_k) \mathbf{P}_{k+1,k} \quad (31)$$

Equation 27 is the prediction step, where the kinematic equations are integrated to obtain the predicted states, which are corrected in the next stage given in Equation 28 using the ADS measurements. In this set of equations, \mathbf{K} is the Kalman gain, \mathbf{H} is the observation matrix, \mathbf{P} is the state covariance matrix, $\mathbf{\Phi}$ is the discrete state transition matrix, $\mathbf{\Gamma}$ is the discrete noise distribution matrix, where \mathbf{Q} and \mathbf{R} are characterized by the input and measurement noise vectors, respectively. The equations below define the linearization, discretization, and noise matrices.

$$\mathbf{F}_k = \left. \frac{\partial \mathbf{f}(\mathbf{x}(t), \mathbf{u}_m(t))}{\partial \mathbf{x}} \right|_{\mathbf{x}=\hat{\mathbf{x}}_{k,k}}, \quad \mathbf{H}_k = \left. \frac{\partial \mathbf{h}(\mathbf{x}(t), \mathbf{u}_m(t))}{\partial \mathbf{x}} \right|_{\mathbf{x}=\hat{\mathbf{x}}_{k,k}} \quad (32)$$

$$\mathbf{\Phi}_k = e^{\mathbf{F}_k \Delta t} = \sum_n \frac{\mathbf{F}_k^n (\Delta t)^n}{n!}, \quad \Delta t = t_{k+1} - t_k \quad (33)$$

$$\mathbf{\Gamma}_k = \int_{t_k}^{t_{k+1}} \mathbf{\Phi}_k \mathbf{N}(\hat{\mathbf{x}}_{k,k}) dt \quad (34)$$

$$\mathbf{Q}_k = E \{ \boldsymbol{\omega}(t)^T \boldsymbol{\omega}(t) \}, \quad \mathbf{R}_k = E \{ \mathbf{v}(t)^T \mathbf{v}(t) \} \quad (35)$$

With these definitions, the state estimation step is complete. By making use of an EKF, the IMU-driven kinematic model and ADS measurements are fused to estimate more accurate states. These states will be used in the following sections for parameter estimation and outer loop flight controllers.

2. Adaptation Method

To estimate and update the control effectiveness model online, it is necessary to employ a parameter estimation strategy. A great candidate for this is the Recursive Least Squares (RLS). Due to its recursive nature, RLS is able to continuously incorporate new data for estimation. Moreover, compared to other estimation approaches such as least-mean-squares, it exhibits faster convergence, which is highly desirable, as flight safety after damage depends heavily on the adaptation speed. However, a limitation of RLS is its equal weighting of recent and past data. This can be problematic for fault-tolerant control design. After damage occurs, new sensor data becomes more valuable as the RLS needs to quickly learn the changes in control effectiveness and update the model. Hence, new data must have larger weight than old data. This issue can be mitigated by using a variable forgetting factor (VFF), which was initially proposed in [22]. Using a VFF allows RLS to keep a constant information content and to follow both slow and sudden changes in control effectiveness. As an example, in the context of aviation, sudden changes can occur due to structural damage, whereas slow changes could be due to in-flight icing of control surfaces. This paper focuses only on the sudden changes.

Looking at Equation 9, it is possible to see that the control effectiveness matrix only contains the coefficient of each surface with respect to the aerodynamic moments. In order to utilize RLS, a regression model for each of these must be set-up. Normally, choosing a regression model is a tedious process that involves trying different structures of varying complexity to find the best fit. Alternatively, this procedure can be streamlined by automating the selection of models online, as suggested in [23]. Fortunately, for the purposes of this study, such procedures are not required. Since the aerodynamic framework employed in the aircraft simulation model originates from [6], its structure is perfectly known. The structure of the moment coefficients is given in Equation 36.

$$C_* = C_{*0} + C_{*\alpha}(\alpha) + C_{*\beta}(\beta) + C_{*p^*}(p^*) + C_{*q^*}(q^*) + C_{*r^*}(r^*) \\ + C_{*\delta_{CS1L}}(\delta_{CS1L}) + C_{*\delta_{CS1R}}(\delta_{CS1R}) + C_{*\delta_{CS2L}}(\delta_{CS2L}) + C_{*\delta_{CS2R}}(\delta_{CS2R}) + C_{*\delta_{CS3}}(\delta_{CS3}) \quad (36)$$

where C_* accounts for C_L , C_M , and C_N . In addition, $p^* = p \frac{c}{\bar{v}}$, $q^* = q \frac{c}{\bar{v}}$, and $r^* = r \frac{c}{\bar{v}}$. This structure is identical to the VLM model used to simulate aircraft dynamics given in [24]. By decomposing this, it is possible to define the following regression and parameter vectors:

$$\mathbf{a}_{k+1} = \begin{bmatrix} 1 & \alpha & \beta & p^* & q^* & r^* & \delta_{CS1L} & \delta_{CS1R} & \delta_{CS2L} & \delta_{CS2R} & \delta_{CS3} \end{bmatrix} \quad (37)$$

$$\hat{\boldsymbol{\theta}}_k = \begin{bmatrix} C_{*0} & C_{*\alpha} & C_{*\beta} & C_{*p^*} & C_{*q^*} & C_{*r^*} & C_{*\delta_{CS1L}} & C_{*\delta_{CS1R}} & C_{*\delta_{CS2L}} & C_{*\delta_{CS2R}} & C_{*\delta_{CS3}} \end{bmatrix} \quad (38)$$

where \mathbf{a}_{k+1} is the regression vector that contains the new measurements and $\hat{\boldsymbol{\theta}}_k$ is the parameter vector that includes estimates of aerodynamic coefficients.

Now that the regression model has been set up, it is necessary to determine the aerodynamic moments acting on the aircraft. Although the aircraft does not have sensors that can directly measure these moments, they can be constructed by utilizing gyroscopes and accelerometers. In Section II.C, it was explained that body accelerations are calculated from body rates using Euler differentiation. Hence, by using the measured angular velocities p_m, q_m, r_m , and the calculated body accelerations $\dot{p}_c, \dot{q}_c, \dot{r}_c$, it is possible to construct the moments acting on the aircraft as the following:

$$L_c = I_{xx}\dot{p}_c - (I_{yy} - I_{zz})q_m r_m - I_{xz}(\dot{r}_c + p_m q_m) \\ M_c = I_{yy}\dot{q}_c - (I_{zz} - I_{xx})r_m p_m - I_{zx}(r_m^2 - p_m^2) \\ N_c = I_{zz}\dot{r}_c - (I_{xx} - I_{yy})p_m q_m - I_{zx}(\dot{p}_c - q_m r_m) \quad (39)$$

assuming a symmetric airframe, $I_{xz} = I_{zx} = 0$. These moments can be nondimensionalized and rewritten in the body fixed reference frame as

$$C_{L_{calc}} = \frac{L_c}{\bar{\rho} S b} \quad C_{M_{calc}} = \frac{M_c}{\bar{\rho} S c} \quad C_{N_{calc}} = \frac{N_c}{\bar{\rho} S b} \quad (40)$$

With these, the aerodynamic moments are derived from the sensor readings. To isolate the contributions of control surfaces to these moments, the regression model and the VFF-RLS algorithm are used to identify the impact of each parameter. For this, the residual of the RLS algorithm is set up as

$$\boldsymbol{\varepsilon}_{k+1} = y_{k+1} - \mathbf{a}_{k+1} \cdot \hat{\boldsymbol{\theta}}_k = y_{k+1} - \hat{y}_{k+1} \quad (41)$$

In this residual, y_{k+1} stands for constructed aerodynamic moments from sensor data, C_{Lcalc} , C_{Mcalc} , and C_{Ncalc} , whereas \hat{y}_{k+1} is the model prediction that comes from the regression and parameter vectors. Hence, the residual can be stated as the difference between the sensed moments and the model-predicted moments. The VFF-RLS algorithm used for this purpose is outlined as

$$1. \text{ RLS gain } \rightarrow \mathbf{K}_{k+1} = \mathbf{P}_k \cdot \mathbf{a}_{k+1}^T \left(\mathbf{a}_{k+1} \cdot \mathbf{P}_k \cdot \mathbf{a}_{k+1}^T + 1 \right)^{-1} \quad (42)$$

$$2. \text{ VFF } \rightarrow \lambda_{k+1} = \max \left\{ 1 - \Sigma_0^{-1} (1 - \mathbf{a}_{k+1} \cdot \mathbf{K}_{k+1}) \cdot \varepsilon_{k+1}^2, \lambda_{min} \right\} \quad (43)$$

$$3. \text{ Parameter update } \rightarrow \hat{\boldsymbol{\theta}}_{k+1} = \hat{\boldsymbol{\theta}}_k + \mathbf{K}_{k+1} \cdot \varepsilon_{k+1} \quad (44)$$

$$4. \text{ Parameter covariance update } \rightarrow \mathbf{P}_{k+1} = \frac{1}{\lambda_{k+1}} (\mathbf{I} - \mathbf{K}_{k+1} \cdot \mathbf{a}_{k+1}) \cdot \mathbf{P}_k \quad (45)$$

λ_{min} is typically chosen to be a constant value to prevent the forgetting factor from becoming negative or too close to zero, which might happen when the residual is large. Σ_0 is a scalar tuning variable, and it is related to the aggressiveness of adaptation, where higher values usually mean slower but robust adaptation.

3. Persistency of Excitation

Proper excitation plays a significant role in online parameter estimation. For identification, each surface must be quickly and sufficiently excited to estimate the contributions of individual control surfaces to the total aerodynamic moments. This is especially important after structural damage to ensure fast and accurate convergence of the estimates. However, an identification routine must guarantee that the aircraft remains stable without significant deviations in flight path or orientation.

Although multiple methods are available for exciting control surfaces, the technique of separate surface excitation (SSE) [21, 25, 26] is favored. This approach facilitates a separate analysis for each surface's identification and avoids undesired correlations during parameter estimation. For the purposes of this study, SSE is implemented as a doublet input with a very short pulse width to approximate a bilateral impulse. As noted in [27], this excitation method is theoretically comprehensive across all frequencies and is easy to implement for online applications.

Since the control surfaces are capable of moving significantly faster than the aircraft itself, it can be assumed that the changes in aerodynamic moments due to the identification maneuver are solely caused by the control deflections. This follows from the time-scale separation principle in the sense that slow aircraft dynamics are assumed to be decoupled from fast actuator dynamics. Of course, this assumption is only valid for a short period of time until the airframe starts to react to the changes caused by the surfaces. Nevertheless, that small time window is sufficient to generate the necessary information for the RLS algorithm that will lead to a successful identification of control effectiveness.

4. Fault Modeling

This study considers two types of fault/damage scenarios. These are loss of control surface area and actuator jamming problems. Based on [28], the loss of control effectiveness is bound to occur due to a physical loss of control surface area. Assuming that the inertia effects resulting from this mass loss are negligible, the fault can be effectively modeled by applying a scaling factor to the control derivatives.

$$C'_{ij} = C_{ij} \mu_j, \quad \mu_j \in [0, 1] \quad (46)$$

where $i = l, m, n$, and $j = \delta_{CS1L}, \delta_{CS1R}, \delta_{CS2L}, \delta_{CS2R}, \delta_{CS3}$, and C' indicates the control derivative after the fault has occurred.

Actuator jamming is slightly less straightforward to model. From previous studies on the Flying-V and other flying-wing type aircraft, it is known that lateral stability and limited directional control authority present a challenge [3, 29]. For this reason, this study only considers elevon hardover. This type of fault has two implications on the aircraft. First, since the actuator is jammed in a fixed position, it will lose all effectiveness to future control inputs, which means the control derivative will be scaled with $\mu_j = 0$. And secondly, when jamming occurs at a non-neutral deflection angle, the surface generates additional moments that must be compensated for by the healthy surfaces. Since the Flying-V uses elevons instead of separate elevators and ailerons, the neutral point for these surfaces are equal to the deflection required to trim the aircraft. Therefore, moments resulting from elevon jamming can be written as

$$\Delta C_l = C_{l,e} \Delta \delta_e \quad \Delta C_m = C_{m,e} \Delta \delta_e \quad \Delta C_n = C_{n,e} \Delta \delta_e \quad (47)$$

where $\Delta\delta_e = \delta_{trim} - \delta_{jam}$ is the difference between the trim and jammed deflection angles.

C. Outer Loop Control Laws

The outer loop consists of the C^* controller, roll and pitch reference models with flight envelope protection (FEP), sideslip compensator, linear controller, and pseudo control hedging. In the context of flight control systems, the outer loop is responsible from converting the pilot inputs into a form that is useful for the inner loop. The flight control architecture used in this paper accepts C^* , roll rate, and sideslip commands from the pilot, and converts them into a virtual control input, v , for the INDI-based inner loop.

1. C^* Longitudinal Controller

For longitudinal control, a control law based on the C^* parameter is chosen [30]. C^* was initially designed as a handling quality criterion following the hypothesis that pilots primarily sense and respond to the load factor and pitch rate of an aircraft. Later, with the incorporation of feedback elements and the advent of fly-by-wire control systems, C^* evolved into a control methodology rather than a handling quality assessment tool. Nowadays, C^* is an umbrella term for longitudinal controllers that utilize a weighted combination of load factor and pitch rate command. The structure of this controller can be given as:

$$C^*_{comm} \frac{\cos\theta}{\cos\phi} = \frac{V}{g}q + n_{zact} \quad (48)$$

where n_{zact} is the aircraft's load factor, V is true airspeed, and q is pitch rate. This structure is slightly different from the original definition of C^* as it includes a lift compensation term $\frac{\cos\theta}{\cos\phi}$, that lowers the commanded load factor at higher pitch angles [15]. An advantage of C^* is its ability to trade-off between load factor and pitch rate. When the aircraft is travelling at the crossover velocity, $V = V_{CO}$, pitch rate and load factor contribute equally to C^* . At lower velocities, the influence of the pitch rate is greater, whereas at higher velocities the load factor predominates. Figure 5 shows the schematic of the C^* algorithm used for the Flying-V. In addition, this structure serves to transform the C^* command

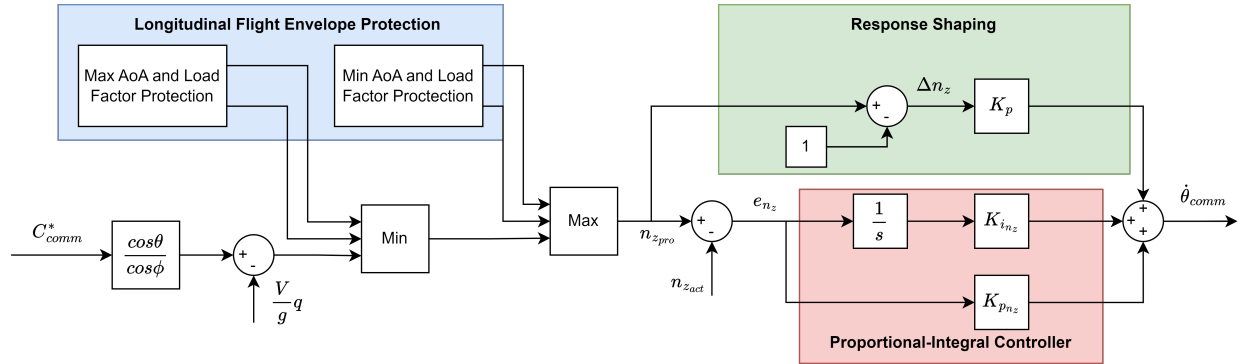


Fig. 5 Schematic of the C^* controller, modified from [5]

given by the pilot into a pitch rate signal for the pitch reference model. This is done by using a proportional-integral approach. The section of the figure inside the blue box covers the longitudinal components of the flight envelope protection. Details of this will be explained in Section III.C.3.

2. Pitch and Roll Reference Models

Fundamentally, both the pitch and roll reference models are second-order filters. Their primary purpose is to convert the commanded pitch and roll rate inputs into pitch and roll reference signals for the linear controller. The key difference between the two models is that the roll reference model contains a roll protection system and acts as a rate control attitude hold (RCAH) controller. Figure 6 gives an overview of the roll reference model. The pitch reference model is identical to this, except for the flight envelope protection section indicated by the blue box. Hence, the pitch reference model is not presented in a separate figure.

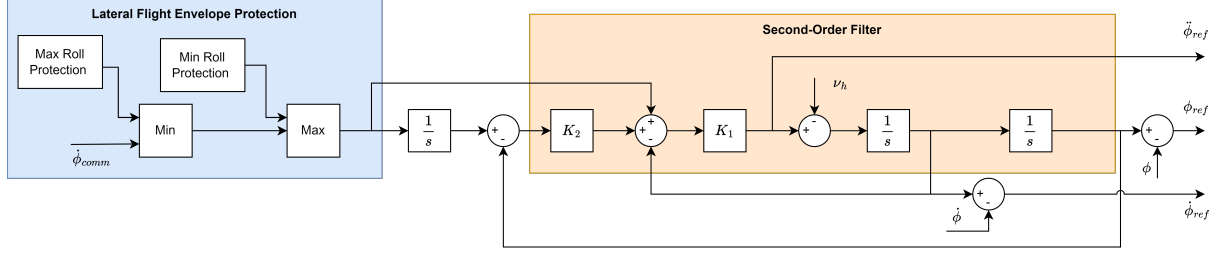


Fig. 6 Schematic of the roll reference model and lateral FEP, modified from [5]

3. Flight Envelope Protection

The flight envelope protection (FEP) consists of two components, longitudinal and lateral FEP. The longitudinal FEP is further subcategorized as the angle of attack (AoA) protection and the load factor protection, both of which work by restricting the load factor component of the C* command.

The angle of attack protection is particularly important for the Flying-V due to the pitch break behavior noted in previous studies [5, 6, 12]. The maximum and minimum load factor based on angle of attack can be defined by using a proportional approach as:

$$n_{z\alpha_{max}} = n_z + K_{\alpha_{max}} (\alpha_{max} - \alpha) \quad \text{and} \quad n_{z\alpha_{min}} = n_z + K_{\alpha_{min}} (\alpha_{min} - \alpha) \quad (49)$$

where α_{max} is a function of altitude, and is linearly interpolated between 22 degrees at sea level and 24 degrees at 13 km altitude. On the other hand, α_{min} is a constant value and is set to -5 degrees. The AoA protection only becomes active when α is larger than 15 or smaller than 0 degrees. Outside of this range, $n_{z\alpha_{max}} = 2.5$ and $n_{z\alpha_{min}} = -1$.

For load factor protection, 2.5 and -1 are considered as global limits. Based on [5, 15], and referring back to Figure 5, the maximum load factor can be written as

$$n_{z_{max}} = \max \left(1, \min \left(2.5, 1 + \frac{(C_{L_{max}} - \Delta C_{L_{max}}) \bar{q} S}{W} \cos \phi - n_y \sin \phi - \cos \gamma + \frac{T}{W} \sin \alpha \cos \phi \right) \right) \quad (50)$$

where $\Delta C_{L_{max}} = 0.01$ and $C_{L_{max}} = 1.7414$ which for this Flying-V model, is equal to the lift coefficient at an AoA of 25 degrees. Following a similar structure, it is possible to define roll and roll rate protections as in Equations 51 and 52.

$$\phi_{max} = \min \left(66, \cos^{-1} \left(\frac{mg \cos \gamma}{T \sin \alpha + (C_{L_{max}} - \Delta C_{L_{max}}) \bar{q} S} \right) \right) \quad (51)$$

As can be seen from this equation, the maximum bank angle is set to 66 degrees. This value indicates an extreme scenario. Under normal flight conditions for a commercial airplane, the bank angle would be expected to remain within ± 35 degrees. Lastly, the roll rate limits can be given as

$$\dot{\phi}_{max} = K_{\phi_{pro}} (\phi_{max} - \phi) \quad \text{and} \quad \dot{\phi}_{min} = K_{\phi_{pro}} (-\phi_{max} - \phi) \quad (52)$$

The roll protection activates only when within 2 degrees of the threshold to avoid interference during normal flight.

4. Sideslip Compensator

The directional control channel relies on a sideslip controller. The sideslip compensator accepts the commanded sideslip from the pilot and produces a reference yaw rate to be used by the linear controller. Figure 7 shows the structure of the sideslip compensator. Based on this figure, the control law can be written as in Equation 53.

$$r_{comm} = \frac{w_p - A_y}{V} - \left(\frac{K_{\beta I}}{s} (\beta_{comm} - \beta) - K_{\beta} \beta \right) \quad (53)$$

5. Linear Controller

Referring to Figures 6 and 7, all reference signals produced by the reference models and the sideslip compensator are essentially errors between the commanded and actual angular positions, velocities, and accelerations. The error

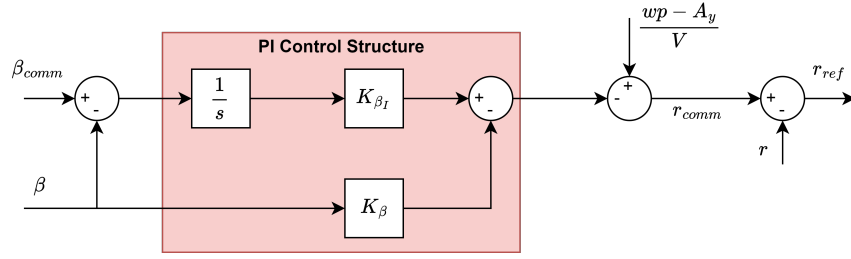


Fig. 7 Schematic of the sideslip compensator, modified from [5, 15]

dynamics can be stabilized by using a linear PI control scheme that generates virtual control inputs for the INDI controller. Since the INDI inner loop is based on angular rate, a virtual control input is needed for each rate term. According to [5, 15] these can be obtained using the following set of equations

$$\begin{aligned}
 v_p &= \left(\frac{1}{s} K_{\phi_I} + K_{\phi} \right) \phi_{ref} + K_{\dot{\phi}} (\dot{\phi}_{ref}) + K_{\ddot{\phi}} (\ddot{\phi}_{ref}) \\
 v_q &= K_{\theta} (\theta_{ref}) + K_{\dot{\theta}} (\dot{\theta}_{ref}) + K_{\ddot{\theta}} (\ddot{\theta}_{ref}) \\
 v_r &= K_r (r_{ref})
 \end{aligned} \tag{54}$$

6. Pseudo Control Hedging

The goal of pseudo control hedging (PCH) is to account for the physical limitations of the control effectors. This is done by scaling the commanded signal down in the reference models, as seen in Figure 6. PCH is an important addition to dynamic inversion based inner loop controllers because the INDI control law, $\Delta \mathbf{u} = \mathbf{G}^{-1}(\mathbf{x}_0, \mathbf{u}_0)(\mathbf{v} - \dot{\mathbf{x}}_0)$, does not consider actuator limitations. Hence, the PCH aims to scale the control input down to a level achievable by the actuators. From [5], the virtual hedge can be calculated as

$$\mathbf{v}_h = \mathbf{G}(\mathbf{x})(\mathbf{u}_{comm} - \mathbf{u}_{real}) \tag{55}$$

where \mathbf{u}_{comm} is the commanded control that serves as input for the actuators, and \mathbf{u}_{real} is the output of the actuators and it is the actual control input that goes into aircraft dynamics.

This concludes the flight control design; Section IV focuses on outlining the simulation setup that includes model configurations, tracking objectives, fault conditions, and the simulation timeline.

IV. Simulation Setup

This section introduces several model configurations, explains the fault cases, and outlines the tracking objectives. Referring back to Figure 4, there are two different representations of the aircraft in the simulation model. The first is the true system dynamics model that characterizes the real aircraft and experiences all structural damages or actuator faults that occur during flight. The second is the onboard control effectiveness model used for control design. The onboard model is made up of lookup tables that contain the control derivatives at pre-determined flight conditions. Data for any flight condition that are not directly available in the table are obtained by linear interpolation between the flight conditions. Consequently, this model has no access to the true dynamics of the system and is not informed about the damage or faults that affect the aircraft.

At this point, the adaptation scheme for the INDI controller becomes instrumental. The control effectiveness estimates calculated using recursive least squares allow updating the onboard model, making it adaptive to the changes in true system dynamics. This essentially minimizes the mismatch between the actual and onboard models, which in turn improves the controller's performance. Table 3 outlines the different model configurations that are simulated.

These four cases identify problems with varying complexity. In case 1, the aircraft does not suffer any damage/faults during flight and the onboard control effectiveness model remains unchanged. Given that the aircraft condition is nominal, there are no discrepancies between the models. In case 2, the aircraft experiences damage/faults; however, the

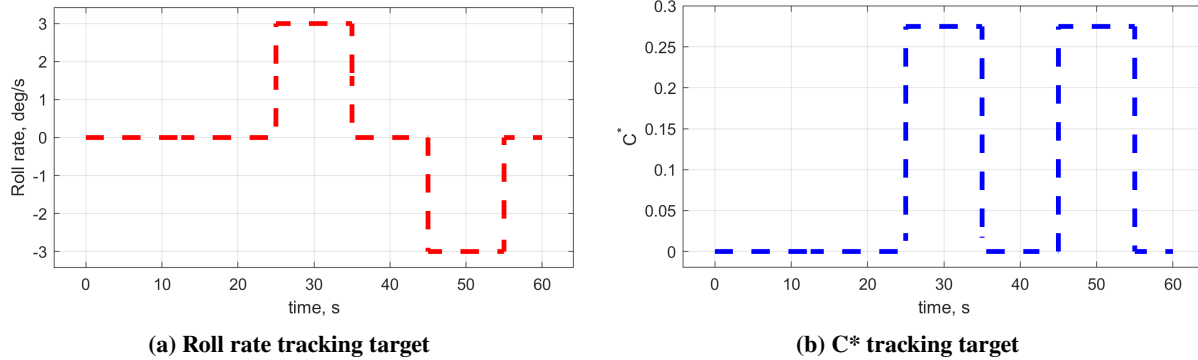
Table 3 Simulation model configurations

Configuration	True Aircraft Dynamics	Onboard Model
1	nominal	nominal
2	with damage or faults	nominal
3	with damage or faults	fault-informed
4	with damage or faults	estimated

onboard model is not informed. This causes a mismatch between the models and is expected to degrade the controller's performance. On the other hand, in case 3, although there are faults or damage present in the system, the onboard model is perfectly informed. This is a hypothetical and optimal scenario, as the onboard model can never have exact knowledge of true system dynamics. Finally, case 4 refers to a nonnominal aircraft with an estimated onboard model, which is the solution proposed in this study.

A. Tracking Objectives

Since the flight control system described in Figure 3 accepts C^* , roll rate, and sideslip commands from the pilot, the tracking signal will be based on C^* and roll rate to assess controller performance. In fact, this can be related to the EASA CS-25 regulations [31]. From CS 25.671(d), in order to demonstrate maneuverability and flight safety under all-engines-out condition, it is possible to use a roll maneuver from a 30 degree bank to -30 degree bank, a pull-up maneuver to 1.3 g and a push-down maneuver to 0.8 g. Although this study does not consider engine failures, similar maneuvers can be employed to demonstrate maneuverability. To this end, two types of tracking objectives are defined.

**Fig. 8 Tracking objectives**

The aircraft is commanded to track either one or both of these tracking targets for the fault cases described in the following subsection. The roll rate tracking is particularly important when there are asymmetrical damages on the wings, where only one side of the aircraft is affected. On the other hand, the simultaneous C^* and roll rate commands become important for quasi-symmetrical actuator failures. An important point is that since the C^* controller contains a turn compensation term as covered in Section III.C.1, the actual C^* command to be tracked is $C_t^* = C^* \frac{\cos \theta}{\cos \phi}$.

B. Fault Conditions

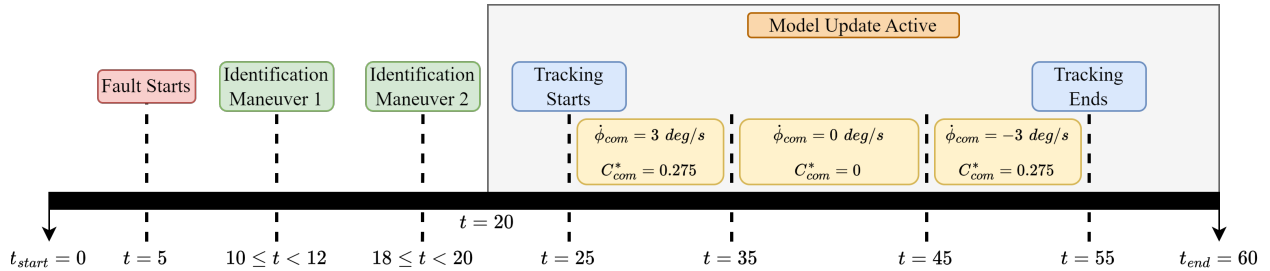
The modeling of damage/fault cases were discussed in Section III.B.4. For this study, two types of fault cases are considered, asymmetrical and quasi-symmetrical. Asymmetrical faults are assumed to occur due to control surface losses. This essentially represents a scenario where one side of the aircraft experiences impact with a foreign object. Quasi-symmetric faults, on the other hand, represent simultaneous jamming of control surfaces on both sides of the aircraft. The right inboard elevon runs away and becomes immobilized at its maximum deflection, whereas the left outboard elevon gets stuck at zero deflection. It is important to note that since the Flying-V requires a positive elevon deflection to trim, zero deflection is not the same as the trim deflection. The list of fault cases is given in Table 4.

Table 4 Fault scenarios

Case	Affected Surface	Failure Type	Period, s	Scaling Factor, μ_j
Asymmetrical	Left inboard elevon (1L)	Loss of control surface	$t \geq 5$	0
	Left outboard elevon (2L)	Loss of control surface	$t \geq 5$	0.875
Jamming position, deg				
Quasi-symmetrical	Right inboard elevon (1R)	Elevon hardover	$t \geq 5$	25
	Left outboard elevon (2L)	Elevon hardover	$t \geq 5$	0

C. Simulation Timeline

This subsection presents the temporal progression of the simulation for all model configurations and fault cases. All simulations follow a similar timeline. After the fault occurs, two subsequent identification maneuvers excite the control surfaces such that the parameter estimation algorithm can assess their effectiveness. After this, adaptation triggers the model update, and the estimated control derivatives begin overwriting the onboard model. It is important to note that model update is only active for the estimated onboard model case, indicated as Configuration 4 in Table 3. This is followed by the roll rate and C^* tracking commands. The simulation timeline is shown in Figure 9.

**Fig. 9** Timeline for the simulations

V. Performance Analysis under Fault Scenarios

This section presents and provides an analysis of the results for the model and fault scenarios outlined in the previous section. Before diving into simulations with faults, the nominal behavior of the aircraft should be addressed. The nominal behavior corresponds to Configuration 1 in Table 3, where both the true aircraft dynamics and the onboard model are free of faults and online adaptations. For the sake of comparison, the simulation for this case retains the identification maneuvers and uses the same tracking signals as the rest of the configurations. The results are given in Figure 10. Based on the figure, the nominal aircraft does not experience difficulties following the reference signals and performing identification maneuvers. However, there are some small jumps in the roll rate and C^* signals during the first 20 seconds of the simulation. Judging from the simulation timeline covered in the previous section, these jumps are due to identification maneuvers.

Another point that requires attention prior to fault simulations is the state estimation. As explained in section III.B.1, an Extended Kalman Filter is used in combination with an air data based kinematic model to utilize redundant sensor information for obtaining more accurate estimates of some aircraft states. The EKF is active for all simulations presented in this paper. However, the estimation results are only shown here to demonstrate the stability and convergence of the filter. These results are given in Figure 11. The estimated states align quite closely with the true states even during maneuvers. In addition, the estimates do not exhibit drift, which ensures the validity of the implementation.

In the following subsections, the term nominal refers to configuration 2, while fault-informed (or informed) to configuration 3, and estimated to configuration 4, as outlined in Table 3.

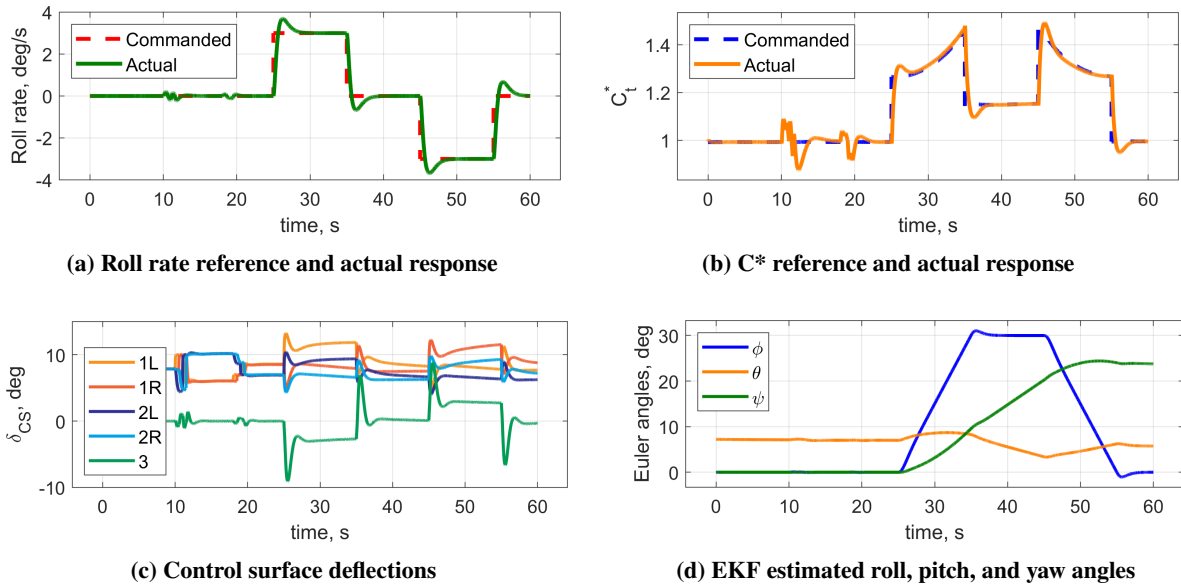


Fig. 10 Nominal model (configuration 1) results

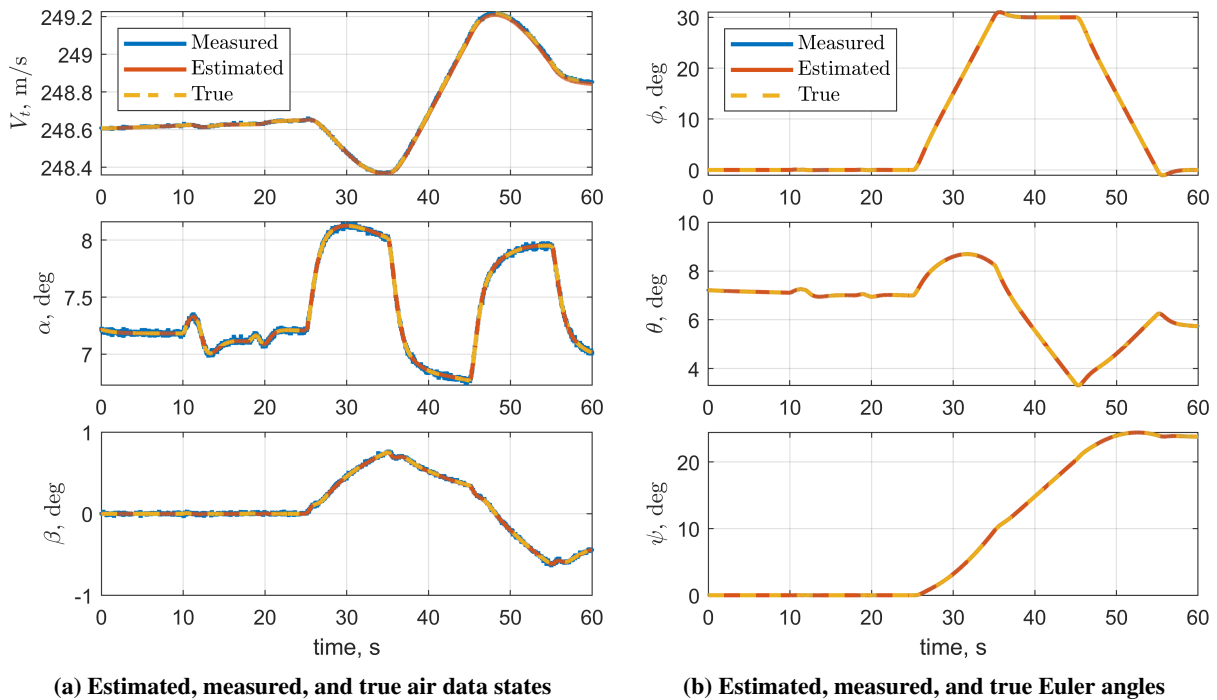


Fig. 11 State estimation results compared with true and measured states

A. Asymmetrical Fault Condition

As outlined in Table 4, this fault condition refers to a situation where the aircraft undergoes loss of control surfaces only on its left side, leading to an asymmetric fault scenario. The tracking objective for this case is only the roll rate reference signal. The reason being is that for asymmetric faults, rolling maneuvers are sufficient to present a challenge to the damaged aircraft; hence, including C^* tracking in addition to roll rate tracking would be infeasible. The roll rate responses using different onboard model configurations are plotted in Figure 12.

Following the simulation timeline, both the start of the fault and the identification maneuvers lead to jumps in roll rate response for all models. The informed and estimated models exhibit a close behavior, whereas the nominal model is

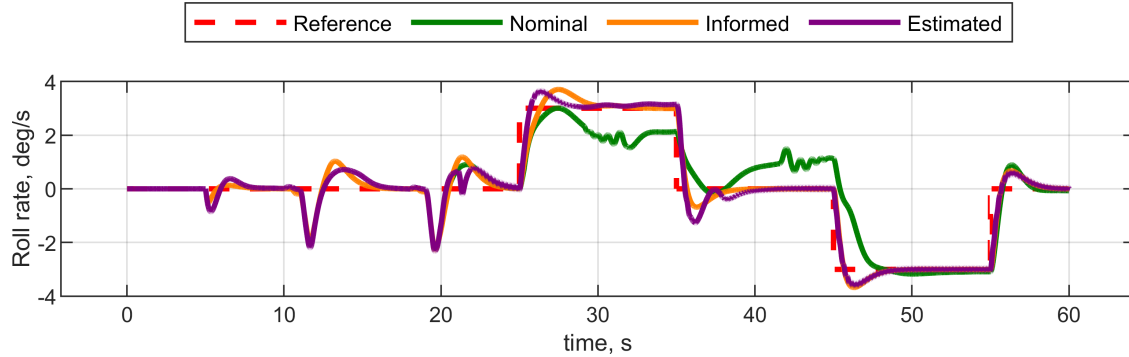


Fig. 12 Roll rate responses for the asymmetric fault condition

not able to follow the reference signal accurately. This result is expected because the nominal onboard model fails to capture the true dynamics of the aircraft, leading to a model mismatch. The comparison of RMSE between the model responses and the reference signal is given in Table 5.

Table 5 RMSE of the roll rate responses for each model configuration

Onboard Model Type	RMSE, deg/s
Nominal	0.8265
Informed	0.5774
Estimated	0.5560

As expected, the nominal model displays a higher error than the informed and estimated cases. However, a surprising outcome is that the estimated model actually outperforms the informed model, showing a lower tracking error. Since the informed model has perfect knowledge of true aircraft dynamics, it is expected to be the most accurate configuration. This would also imply that since the informed model knows how effective the control surfaces are, it can avoid using excessively small or large control deflections to follow the tracking signal and provide a well-dampened response. Based on this, the informed model outperforming the estimated model can be explained by the discrepancy between the true and estimated control moment coefficients. Figure 13 provides these coefficients for damaged control surfaces under asymmetric fault.

For surface 1L, all moment coefficients successfully converge to the true values. On the other hand, judging from 13b, the rolling and yawing moment coefficients for surface 2L are underestimated. The underestimation of control effectiveness causes the INDI controller to calculate larger than necessary control deflections to follow the tracking signal. This in turn leads to a faster aircraft response compared to the informed case. Hence, by underestimating control effectiveness, the aircraft is able to follow the tracking signal more closely. However, this comes at the cost of artificially increasing the control effort. Figure 14 shows the control surface deflections for each model configuration, as well as the Euler angles estimated by the EKF.

As anticipated, the estimated model leads to larger and more oscillatory control deflections compared to the fault-informed model, while the nominal model experiences complete saturation of the damaged surfaces for a large portion of the simulation and the rolling maneuver. This is caused by the mismatch between the onboard and true aircraft model.

B. Quasi-symmetrical Fault Condition

In this fault condition, the aircraft experiences elevon hardover on both sides. However, since the jamming positions are different and the affected surfaces on the left and right sides are outboard and inboard, respectively, it is referred to as quasi-symmetrical. In contrast to the asymmetric case, the tracking objective includes a combination of roll rate and C^* . Since there is at least one undamaged control surface on both sides of the aircraft, roll rate tracking itself does not constitute a sufficient challenge. Figure 15 presents the roll rate and C^* responses of the aircraft for different model configurations.

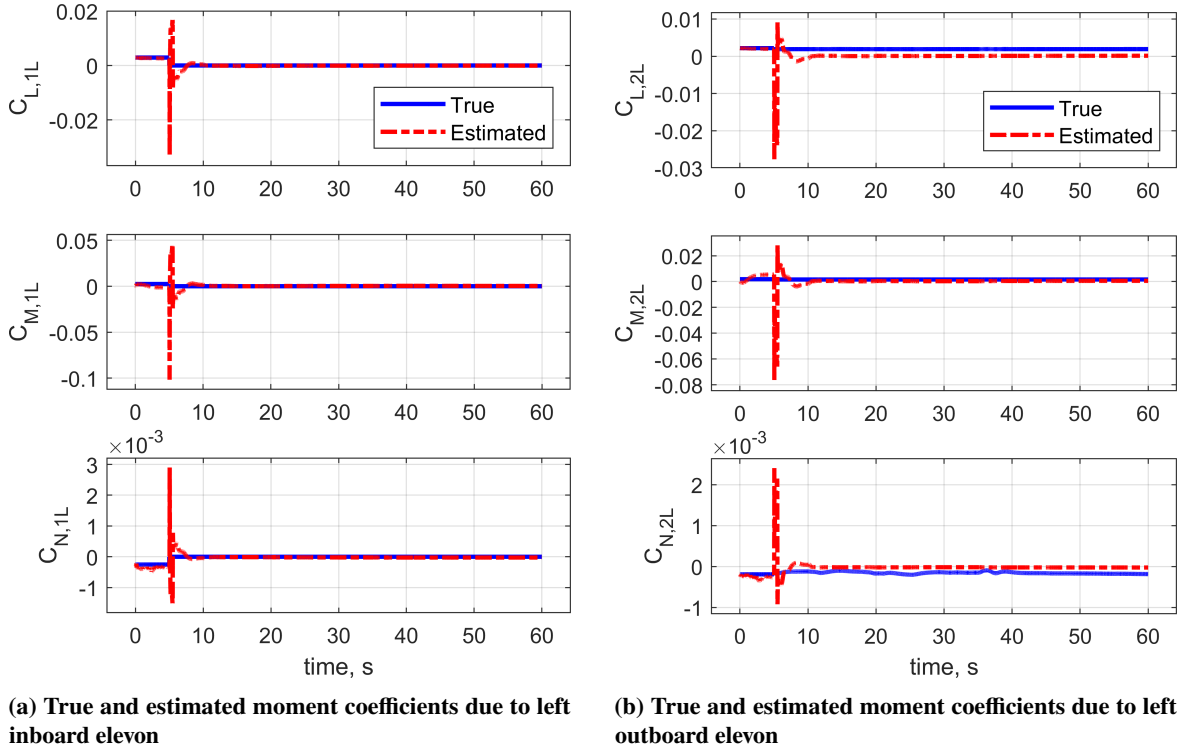


Fig. 13 Moment coefficients of the damaged surfaces for the asymmetrical fault condition

Although the nature of the fault is different, the results resemble the asymmetric case. The core difference being that none of the model configurations is able to follow the roll rate reference accurately between 30 and 40 seconds of the simulation. This implies that this tracking signal is demanding beyond the capability of the damaged aircraft. However, both the informed and estimated models are closely aligned, whereas the nominal model shows a larger deviation from the reference. To investigate the responses in terms of performance criteria, the RMSE of the C^* and roll rate responses are given in Table 6. Expectedly, the nominal model leads the largest error among all models. The estimated model

Table 6 RMSE of the tracking responses for each model configuration

Onboard Model Type	Roll rate RMSE, deg/s	C^* RMSE
Nominal	0.8214	0.3798
Informed	0.7550	0.3456
Estimated	0.7530	0.3549

performs quite close to the informed model, indicating that the control effectiveness parameters are correctly estimated. The true and estimated moment coefficients for the affected control surfaces are given in Figure 16. Since the affected surfaces lose all their effectiveness to future control inputs due to being stuck at a fixed deflection angle, their true coefficients become zero after the fault occurs. This is captured quite well by the estimation algorithm, as the parameters rapidly converge to zero during the first identification maneuver.

As a consequence of elevon hardover, there will be a discrepancy between the actual and commanded control deflections. Even though the surfaces are stuck at a certain angle, the controller does not have access to this information and will try to send command signals to these surfaces. The comparison of the commanded and actual control deflections is given in Figure 17.

At $t = 5$ seconds, 1R runs away and settles at the actuator deflection limit, whereas 2L returns to its zero position. As explained in Section IV.B, the zero position of the surface is different from the trim deflection. Since the Flying-V requires a positive elevon deflection to trim, 2L produces a constant clockwise rolling moment. For the nominal model,

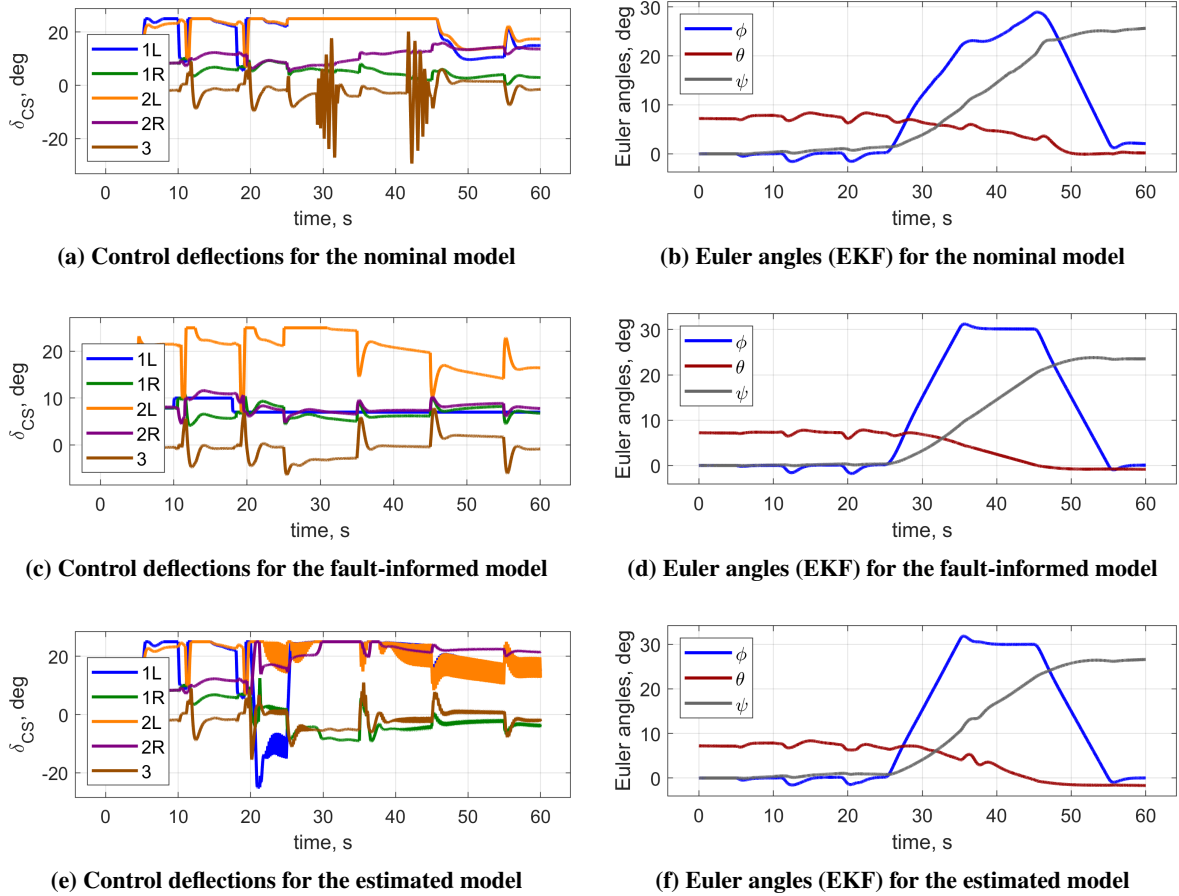


Fig. 14 Control surface deflections and estimated Euler angles for the asymmetrical fault condition

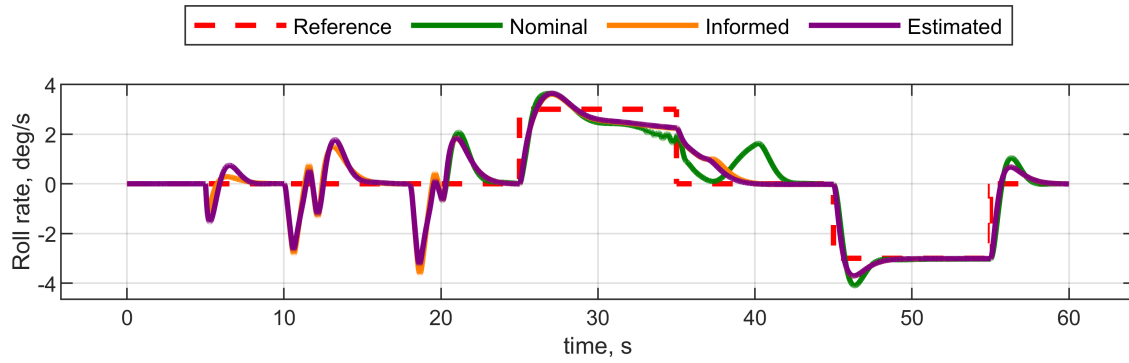
the controller tries sending commands to both 1R and 2L, which causes other control surfaces to saturate since the deflection commands sent to the damaged surfaces are not realized. On the other hand, although there are differences between the commanded and actual deflections, the informed model does not use damaged surfaces to maneuver the aircraft and prioritizes the remaining surfaces. This minimizes the saturation experienced by the active surfaces. Lastly, the estimated model acts similarly to the informed model. During the initial phases of the simulation, it tries utilizing the damaged surfaces; nevertheless, once the parameter estimates converge, it adapts the deflections to prioritize the healthy surfaces.

Finally, the estimated Euler angles using the EKF are depicted in Figure 18. All configurations exhibit similar behavior with some small oscillations in the nominal model.

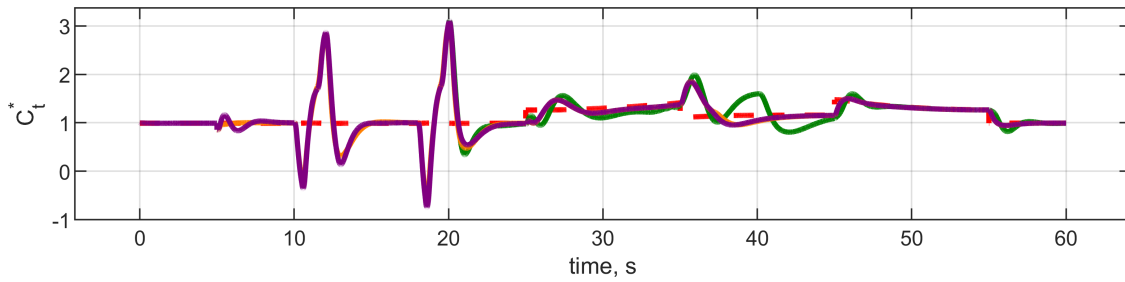
VI. Conclusions

This research focused on proposing a fault-tolerant flight control system for the Flying-V aircraft under actuator faults and structural damage. Such faults or damages cause changes in the true dynamics of the aircraft. However, the onboard control effectiveness models used for classical or non-adaptive INDI-based flight controllers have a fixed structure and cannot adapt to any changes in the true aircraft model, leading to mismatches that degrade the performance of the controller.

To alleviate this problem, a fault-tolerant flight control system is proposed for the Flying-V aircraft, utilizing a two-step state and parameter estimation strategy. In the first stage, an Extended Kalman Filter with an air-data based kinematic model is employed to accurately estimate certain aircraft states. These states are then used in combination with raw IMU measurements in the second stage for parameter estimation. To this end, a Recursive Least Squares

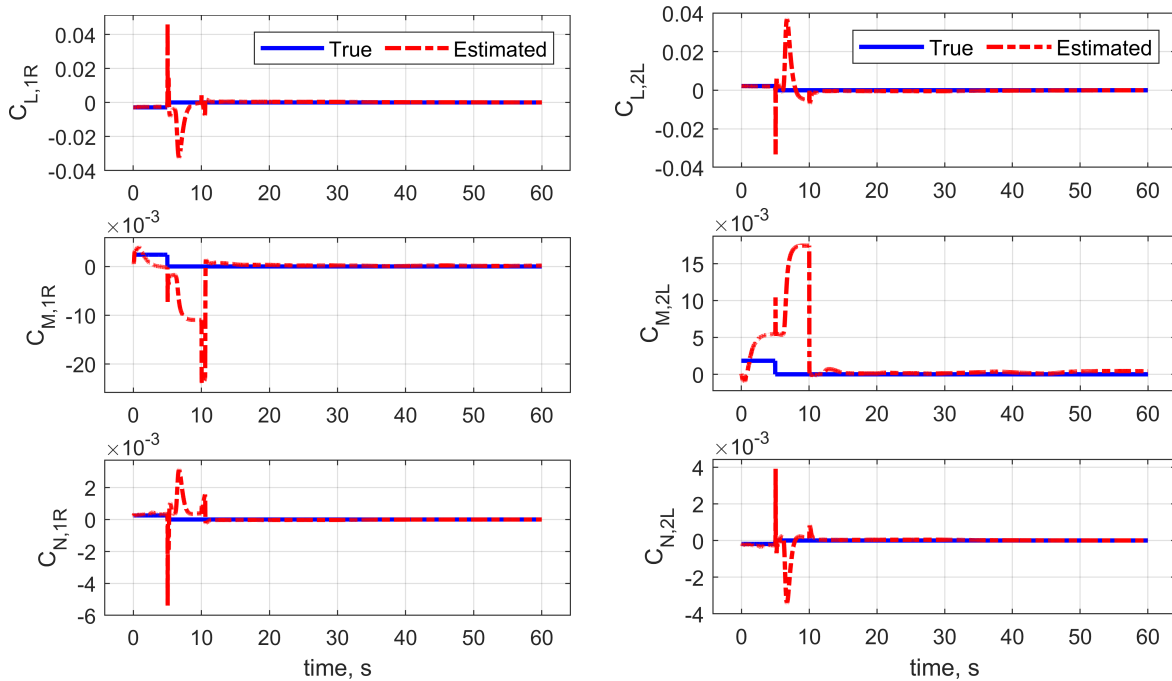


(a) Roll rate responses for the quasi-symmetric fault condition



(b) C_t^* responses for the quasi-symmetric fault condition

Fig. 15 Tracking performance comparison between the models under quasi-symmetrical fault



(a) True and estimated moment coefficients due to right inboard elevon

(b) True and estimated moment coefficients due to left outboard elevon

Fig. 16 Moment coefficients of the damaged surfaces for the quasi-symmetric fault condition

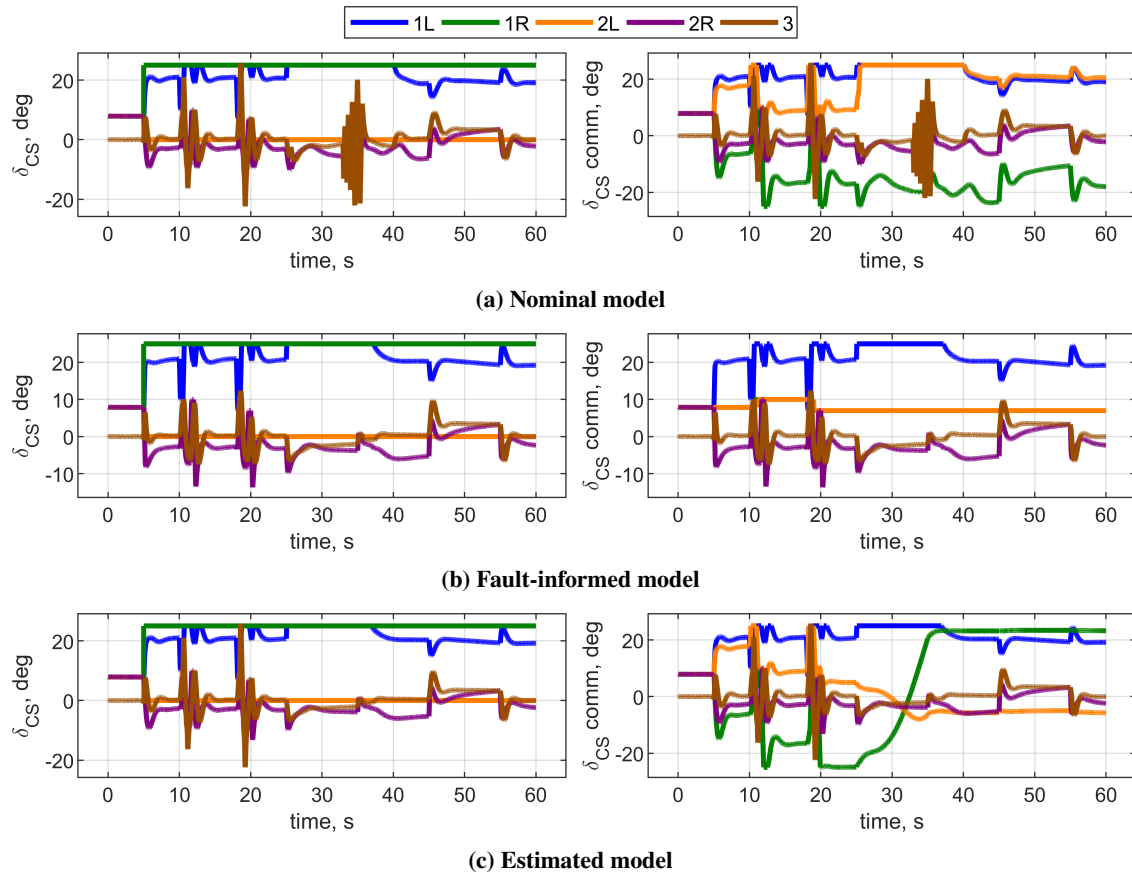


Fig. 17 Comparison of actual (left) and commanded (right) control deflections under quasi-symmetric faults

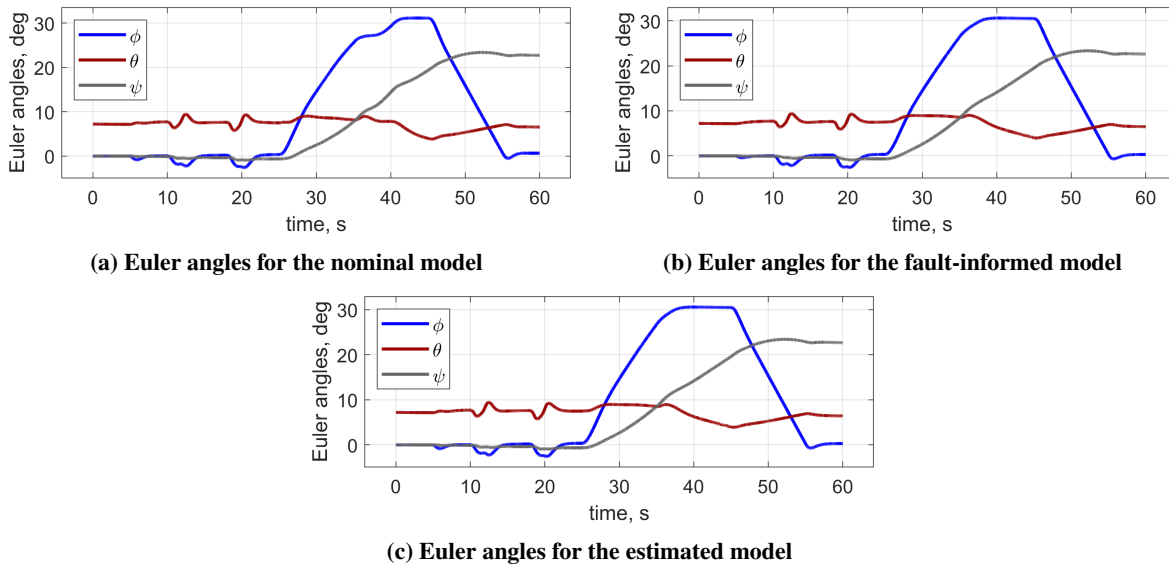


Fig. 18 Estimated Euler angles for all model configurations under quasi-symmetric fault

algorithm with Variable Forgetting Factor (VFF-RLS) is preferred because of its fast adaptation properties. In this stage, sensor measurements are used to calculate the forces and moments that act on the aircraft. Then a regression model is fitted to the moments to estimate and decompose the different parameters contributing to them. The estimated

parameters are used to continuously update the onboard control effectiveness matrix. Hence, this adaptation of the onboard model leads to an Adaptive-INDI control design.

In order to demonstrate the strength of the proposed control system, several model configurations and fault cases are defined. The model configurations are nominal, informed, and estimated, whereas the fault cases are asymmetric and quasi-symmetric. The results showed that with a nominal model, although it remained stable, the aircraft failed to track the reference signals. On the other hand, with an informed or estimated model, it was able to complete the tracking objectives with good accuracy. It should be noted that the informed model is a hypothetical scenario in which the onboard model has perfect knowledge of all faults and damages that the aircraft experiences. Consequently, the informed model is expected to lead to the lowest tracking error.

Interestingly, for the asymmetric fault case, the results showed that in fact the estimated model outperformed the informed model. Although this might seem counterintuitive at first glance, its explanation lies in parameter estimation. It was observed that under that specific fault condition, the rolling moment coefficient for one of the damaged surfaces was underestimated. This led the controller to use higher than necessary control deflections to command the aircraft to track the signal. However, since the actual effectiveness of the surface is larger, the response had a smaller settling time and therefore a lower tracking error. Unfortunately, this came at the cost of artificially increasing control effort and introducing small-amplitude oscillations to control inputs. Another explanation for the estimated model outperforming the informed model could be due to the step nature of the tracking signals. In theory, a smoother tracking signal could reduce the difference in response between the estimated and informed aircraft models. The reason being is that a smoother signal would require a gradual change in control deflections, which would minimize the impact of rolling moment underestimation.

Many recommendations can be given for future research. First, inertial effects are assumed to be negligible for modeling control surface losses in this study. Realistically, structural losses such as this will shift the center of gravity (CG) of the aircraft. The shift in CG and the reformulation of the equations of motion at the new CG location can be considered in a subsequent research activity. Secondly, the excitation used for the identification of the control surface was based on an impulsive doublet input. This was chosen for its low application complexity and reliable performance. However, it could be interesting to conduct further research into an optimal excitation strategy that minimizes disturbance to aircraft while maximizing the estimation convergence after fault or damage. Another possible extension to this work could be related to the adaptation trigger. In this study, the fault was assumed to be known, and the trigger to start updating the onboard model was manually set at a fixed time. It would be a relevant and intriguing extension to conduct research into automating this trigger. Yet another possibility is including the effect of turbulence. Considering that state estimation is performed through an air-data-based kinematic model, involving turbulence could disrupt state estimation. Lastly, IMU and air-data sensors were assumed to be fault-free in this study. Including faults in these sensors would have immediate consequences in the state estimation step and, by extension, in parameter estimation. Therefore, conducting research on methods to detect and address these faults would be relevant.

Acknowledgments

This publication is part of the project Flying V Flight Control with project number 19511 of the Open Technology Program, which is (partly) financed by the Dutch Research Council (NWO). The authors would like to acknowledge the in-kind contributions to the project of KLM Royal Dutch Airlines and ADSE.

References

- [1] Benad, J., "The Flying V - A new Aircraft Configuration for Commercial Passenger Transport," *Deutscher Luft- und Raumfahrtkongress*, Deutsche Gesellschaft für Luft- und Raumfahrt - Lilienthal-Oberth e.V., Bonn, 2015. <https://doi.org/10.25967/370094>.
- [2] Atmaca, D., Stroosma, O., and van Kampen, E.-J., "Piloted Evaluation of Flying-V with Incremental Nonlinear Dynamic Inversion and Envelope Protection," *AIAA SciTech Forum*, Orlando, FL, 2025.
- [3] Joosten, S., Stroosma, O., Vos, R., and Mulder, M., "Simulator Assessment of the Lateral-Directional Handling Qualities of the Flying-V," *AIAA SciTech Forum*, National Harbor, MD, 2023. <https://doi.org/10.2514/6.2023-0906>.
- [4] Torelli, R., Stroosma, O., Vos, R., and Mulder, M., "Piloted Simulator Evaluation of Low-Speed Handling Qualities of the Flying-V," *AIAA SciTech Forum*, National Harbor, MD, 2023. <https://doi.org/10.2514/6.2023-0907>.

- [5] Stougie, J., Pollack, T., and van Kampen, E.-J., “Incremental Nonlinear Dynamic Inversion control with Flight Envelope Protection for the Flying-V,” *AIAA SciTech Forum*, Orlando, FL, 2024. <https://doi.org/10.2514/6.2024-2565>.
- [6] van Overeem, S., Wang, X., and van Kampen, E.-J., “Handling Quality Improvements for the Flying-V Aircraft using Incremental Nonlinear Dynamic Inversion,” *AIAA SciTech Forum*, National Harbor, MD, 2023. <https://doi.org/10.2514/6.2023-0105>.
- [7] Chang, J., De Breuker, R., and Wang, X., “Active Fault-Tolerant Incremental Sliding-Mode Flight Control Against Control Reversal,” *Journal of Guidance, Control, and Dynamics*, Vol. 45, No. 12, 2022, pp. 2411–2420. <https://doi.org/10.2514/1.G006690>.
- [8] Smeur, E. J. J., Chu, Q., and de Croon, G. C. H. E., “Adaptive Incremental Nonlinear Dynamic Inversion for Attitude Control of Micro Air Vehicles,” *Journal of Guidance, Control, and Dynamics*, Vol. 39, No. 3, 2016, pp. 450–461. <https://doi.org/10.2514/1.G001490>.
- [9] Smit, B., Pollack, T., and van Kampen, E.-J., “Adaptive Incremental Nonlinear Dynamic Inversion Flight Control for Consistent Handling Qualities,” *AIAA SciTech Forum*, San Diego, CA, 2022. <https://doi.org/10.2514/6.2022-1394>.
- [10] Cappuyns, T., *Handling Qualities of a Flying V Configuration*, MSc Thesis, Delft University of Technology, 2019. URL <http://resolver.tudelft.nl/uuid:69b56494-0731-487a-8e57-cec397452002>.
- [11] Ruiz Garcia, A., Vos, R., and de Visser, C., “Aerodynamic Model Identification of the Flying V from Wind Tunnel Data,” *AIAA SciTech Forum*, Virtual Event, 2020. <https://doi.org/10.2514/6.2020-2739>.
- [12] van Overeem, S., Wang, X., and van Kampen, E.-J., “Modelling and Handling Quality Assessment of the Flying-V Aircraft,” *AIAA SciTech Forum*, San Diego, CA, 2022. <https://doi.org/10.2514/6.2022-1429>.
- [13] Matamoros, I., and de Visser, C. C., “Incremental Nonlinear Control Allocation for a Tailless Aircraft with Innovative Control Effectors,” *2018 AIAA Guidance, Navigation, and Control Conference*, Kissimmee, FL, 2018. <https://doi.org/10.2514/6.2018-1116>.
- [14] “Type-Certificate Data Sheet No. EASA.E.111 for Trent XWB series engines,” Tech. rep., European Union Aviation Safety Agency, 2022. URL <https://www.easa.europa.eu/en/document-library/type-certificates/engine-cs-e/easae111-rolls-royce-deutschland-trent-xwb-series>.
- [15] Lombaerts, T., Looye, G., Ellerbroek, J., and y Martin, M. R., “Design and Piloted Simulator Evaluation of Adaptive Safe Flight Envelope Protection Algorithm,” *Journal of Guidance, Control, and Dynamics*, Vol. 40, No. 8, 2017, pp. 1902–1924. <https://doi.org/10.2514/1.G002525>.
- [16] Durham, W., A. Bordignon, K., and Beck, R., *Aircraft Control Allocation*, John Wiley & Sons, Ltd, 2017. <https://doi.org/10.1002/9781118827789>.
- [17] Lu, P., van Eykeren, L., van Kampen, E.-J., de Visser, C. C., and Chu, Q. P., “Aircraft inertial measurement unit fault identification with application to real flight data,” *Journal of Guidance, Control, and Dynamics*, Vol. 38, No. 12, 2015, pp. 2467–2475. <https://doi.org/10.2514/1.G001247>.
- [18] van Eykeren, L., and Chu, Q. P., “Sensor fault detection and isolation for aircraft control systems by kinematic relations,” *Control Engineering Practice*, Vol. 31, 2014, pp. 200–210. <https://doi.org/10.1016/j.conengprac.2014.02.017>.
- [19] Lu, P., van Eykeren, L., van Kampen, E.-J., de Visser, C. C., and Chu, Q. P., “Adaptive Three-Step Kalman Filter for Air Data Sensor Fault Detection and Diagnosis,” *Journal of Guidance, Control, and Dynamics*, Vol. 39, No. 3, 2016, pp. 590–604. <https://doi.org/10.2514/1.G001313>.
- [20] Lu, P., van Kampen, E. J., de Visser, C., and Chu, Q., “Nonlinear aircraft sensor fault reconstruction in the presence of disturbances validated by real flight data,” *Control Engineering Practice*, Vol. 49, 2016, pp. 112–128. <https://doi.org/10.1016/j.conengprac.2016.01.012>.
- [21] Lombaerts, T., “Fault Tolerant Flight Control: A Physical Model Approach,” Ph.D. thesis, Delft University of Technology, 2010. URL <https://repository.tudelft.nl/islandora/object/uuid%3A538b0174-fe84-43af-954d-02f256b2ec50?collection=research>.
- [22] Fortescue, T. R., Kershenbaum, L. S., and Ydstie, B. E., “Implementation of self-tuning regulators with variable forgetting factors,” *Automatica*, Vol. 17, No. 6, 1981, pp. 831–835. [https://doi.org/10.1016/0005-1098\(81\)90070-4](https://doi.org/10.1016/0005-1098(81)90070-4).
- [23] Lombaerts, T. J. J., van Oort, E. R., Chu, Q. P., Mulder, J. A., and Joosten, D. A., “Online Aerodynamic Model Structure Selection and Parameter Estimation for Fault Tolerant Control,” *Journal of Guidance, Control, and Dynamics*, Vol. 33, No. 3, 2010, pp. 707–723. <https://doi.org/10.2514/1.47256>.

- [24] van Overeem, S., *Modelling, Control, and Handling Quality Analysis of the Flying-V*, MSc Thesis, Delft University of Technology, 2022. URL <https://resolver.tudelft.nl/uuid:7fd04ecc-41d4-4967-b246-89fdfac2446e>.
- [25] Hamel, P. G., and Jategaonkar, R. V., “Evolution of flight vehicle system identification,” *Journal of Aircraft*, Vol. 33, No. 1, 1996, pp. 9–28. <https://doi.org/10.2514/3.46898>.
- [26] Weiss, S., Friehmelt, H., Plaetschke, E., and Rohlf, D., “X-31A system identification using single-surface excitation at high angles of attack,” *Journal of Aircraft*, Vol. 33, No. 3, 1996, pp. 485–490. <https://doi.org/10.2514/3.46970>.
- [27] Morelli, E., “In-flight system identification,” *23rd Atmospheric Flight Mechanics Conference*, Boston, MA, 1998. <https://doi.org/10.2514/6.1998-4261>.
- [28] Wang, X., van Kampen, E.-J., Chu, Q., and Lu, P., “Incremental Sliding-Mode Fault-Tolerant Flight Control,” *Journal of Guidance, Control, and Dynamics*, Vol. 42, No. 2, 2019, pp. 244–259. <https://doi.org/10.2514/1.G003497>.
- [29] Ammar, S., Legros, C., and Trépanier, J.-Y., “Conceptual design, performance and stability analysis of a 200 passengers Blended Wing Body aircraft,” *Aerospace Science and Technology*, Vol. 71, 2017, pp. 325–336. <https://doi.org/10.1016/j.ast.2017.09.037>.
- [30] Field, E., “The application of a C* flight control law to large civil transport aircraft,” Tech. rep., College of Aeronautics, Cranfield Institute of Technology, Cranfield, England, UK, 1993. URL <https://dspace.lib.cranfield.ac.uk/handle/1826/186>.
- [31] “Easy Access Rules for Large Aeroplanes (CS-25),” Tech. rep., European Union Aviation Safety Agency, 2022. URL <https://www.easa.europa.eu/en/document-library/easy-access-rules/easy-access-rules-large-aeroplanes-cs-25>.